2022-08-09

Measuring Nonlinear Thomson Scattering at Arbitrary Emission Angles

Mahonri Romero Carranza
Brigham Young University

Measuring Nonlinear Thomson Scattering at Arbitrary Emission Angles

Mahonri Romero Carranza

A thesis submitted to the faculty of
Brigham Young University
in partial fulfillment of the requirements for the degree of

Master of Science

Justin Peatross, Chair
Michael Ware
Richard L. Sandberg

Department of Physics and Astronomy

Brigham Young University

ABSTRACT

Measuring Nonlinear Thomson Scattering at Arbitrary Emission Angles

Mahonri Romero Carranza
Department of Physics and Astronomy, BYU
Master of Science

We use photon-counting to measure nonlinear Thomson scattering from low-density electrons in an intense laser focus. The azimuthal and longitudinal polarization components of the second harmonic are measured across much of the full emission sphere. The data show, for the first time experimentally, emission structure in the 'Northern' and 'Southern' hemispheres, where the 'North Pole' aligns with the direction of laser propagation.

To obtain these measurements, we installed an additional power amplifier on our Ti:sapphire laser system at BYU. The upgrade delivers ten times more energy to the laser focus than we had previously. This increase comes partly from the additional amplifier and partly from increased grating efficiency in our pulse compressor. We achieve an on-target pulse energy of 200 mJ at 35 fs. The focal spot size has radius $w_0 = 4\ \mu m$. This corresponds to an available peak intensity of over 10^{19} W/cm^2, an order of magnitude above the onset of strong relativistic effects.

The interaction region in the laser focus has a length of approximately 100 μm. Photons scattered from this region are collected using a 5-cm-focal-length lens and then focused onto the end of a 100-μm-diameter fiber by a second identical lens. The imaging system requires precise alignment with the laser focus, which must be maintained when rotating the photon-collection system along the longitudinal direction of the emission sphere. We developed an alignment procedure that ensures that the detector rotation axis aligns with region of space that is imaged onto the fiber. This region is then aligned to the laser focal spot.

Keywords: Thomson scattering, nonlinear, femtosecond-pulse laser, high-intensity laser

ACKNOWLEDGMENTS

First, I would like to thank my wife Isis and my two children, Ihan and Mia, for their support, time, and sacrifice along this journey. They were my motivation to become a better person. I also would like to thank Scott and Lynn Pelichoff and their family for the support they gave to my family and my education.

At last, I would like to thank my committee and advisers Dr. Peatross, Dr. Ware, and Dr. Sandberg for their support and feedback as I learned to become a better researcher, student, and individual. I am grateful for the knowledge they shared to me as I progressed in my master's program. Their advise will guide as I move forward with my professional career.

Contents

Chapter 1

Introduction

1.1 Free Electron Motion in an Intense Laser Field

The interaction of a free electron with an electromagnetic field was investigated theoretically many decades ago [1–5]. A free electron responds to an incident electromagnetic field in accordance with the Lorentz force law:

$$\vec{F} = e(\vec{E} + \vec{v} \times \vec{B}) \tag{1.1}$$

In the long-wavelength limit (i.e. Thomson scattering as opposed to Compton Scattering), we may neglect any radiation-reaction force as the electron scatters light. That is, we assume that the force of the incident light field on the electron is the dominate one.

At low intensities, the magnetic field component in (1.1) may be be neglected since, in a plane-wave field the strength of the magnetic field is $B = \frac{E}{c}$, whereas v is likely to remain small compared is the speed of light c. In this non-relativistic limit, the electron is driven solely by the electric field. In the case of linearly polarized light, the electron oscillates along a line in simple harmonic motion. Radiation scattered by an electron executing such motion is called Thomson scattering, worked out in 1906 by J. J. Thomson, [1] who discovered the existence of the electron in the first

place. In contrast, at higher intensities, where the electron velocity v can approach c, the magnetic component cannot be neglected, and the motion of the electron is no longer one dimensional, nor linear. Nonlinear Thomson scattering refers to radiation scatter by electrons undergoing such relativistic motion.

The relativistic motion of an electron in an intense electromagnetic plane wave was worked out as early as 1935 by Volkov in the context of a quantum plane wave (representing an electron) interacting with an electromagnetic field [6]. Later in 1951, the behavior of a classical point charge in a strong plane-wave field was described by Landau and Liftshitz [2]. By retaining the magnetic field and accounting for relativistic effects, they demonstrated that an electron executes periodic figure-8 motion in its average rest frame for a linearly polarized monochromatic plane wave. They developed parametric equations for the derivatives that can be solved for the electron motion.

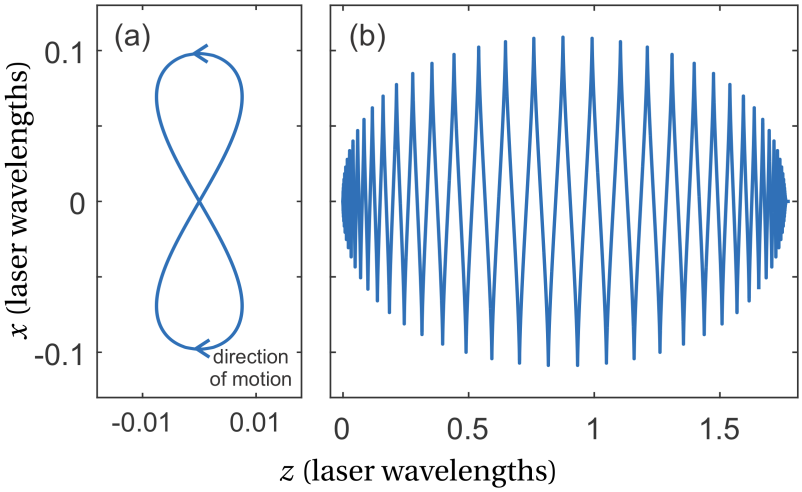

Figure 1.1 Figure-8 motion of an electron in an a linearly polarized laser field with field strength $E = \frac{mc\omega}{e}$, where m and e are the electron charge and mass, c the speed of light, and ω the laser frequency. The electron trajectory is shown (a) in the electron average rest frame for a single cycle near the peak of a pulse and (b) in the lab frame during an entire short laser pulse (with about a dozen cycles in duration). Reproduced from Ref. [23].

In 1962, Vachaspati showed that the electron figure-8 motion contains harmonics of the fundamental driving field [3]. In 1968, Eberly and Sleeper showed that an electron experiencing a laser

pulse is pushed forward by the field so that it drifts along the direction of laser propagation [4]. In 1970, Sarachik and Schappert made an in-depth analysis of nonlinear Thomson scattering arising from this motion. In their paper, they made calculations of what can be observed in a frame that drifts along with the electron (wherein the electron executes the figure-8 motion). They noted that the radiation emitted by the electron in the (average) electron-rest frame has to be transformed to find what is observed in the lab frame [5].

1.2 Nonlinear Thomson Scattering

As mentioned, J.J. Thomson over a century ago first worked out the scattering of radiation by an electron in a plane-wave field, in the linear-response regime [1]. In a linearly polarized field, the harmonic motion of the electron produces a dipole radiation pattern described in many introductory physics textbooks.

At higher intensities, the electron motion becomes nonlinear. Vachaspati showed that the electron figure-8 trajectory produces harmonics [3]. He defined the electric field vector as $\vec{E} = \vec{E}_0 \cos(kz - \omega t)$ and the magnetic field vector as $\vec{B} = \vec{B}_0 \cos(kz - \omega t)$. In a perturbative approach, the electron velocity $\vec{v}$ is considered to be driven solely by the driving electric field $\vec{E}$. Then the $\vec{v} \times \vec{B}$ term gives rise to oscillations along the propagation direction of the driving plane wave with frequency 2ω. Vachaspati then derived the amount of 2nd-harmonic radiation emitted by an electron that experiences this motion. The radiation contains both odd and even harmonics. Again, the self-force on the electron due to emitting radiation is extremely small and can be neglected.

Eberly and Sleeper considered the realistic scenario where the driving field is a quasi-monochromatic plane wave that turns on and turns off [4]. In their analysis, the electron in the lab frame is seen to drift forward along the propagation direction of the incident driving laser pulse, while the electron executes the figure-8 motion. They computed the effective change in the mass for the electron that

arises when the electron motion approaches the speed of light. Viewed at wide angles, the scattered radiation is strongly redshifted due to the electron chasing the driving field.

Sarachik and Schappert calculated harmonic emission in the electron-drift frame per unit solid angle. They showed that in the limit of low intensity, their solution reduces to linear Thomson scattering. They expressed their solution as an infinite series of Bessel functions, since they did their work before computers could easily compute the radiation integral. They also demonstrated that radiation in the electron drift frame corresponds to that of a synchrotron if the incident light is circularly polarized, causing the electron to execute circular motion. In the lab frame, the motion is not periodic and hence is modified from that of pure harmonic generation [5]. To get the radiation in the lab frame, one can apply a Lorentz boost, utilizing the electron drift velocity.

In 1993, Esarey *et al.* analyzed nonlinear Thomson scattering for linearly and for circularly polarized light fields and electrons with arbitrary initial energy [7]. In the same year, Castillo-Herrera *et al.* developed simplified approximate solutions in which they reexamined the work of Sarachik and Schappert work for higher harmonics [8], They showed angular patterns for lower harmonics and considered plasma effects. In both analyses, they compute the intensity of the emitted radiation, including separate polarization components of the scattered light.

Although Sarachik and Schappert produced a robust explanation to the theory of nonlinear Thomson scattering, they did not consider the influence of a laser focus on the electron motion. In 1992, Mohideen *et al.* took the geometry of a tight laser focus into account for an interaction of a free electron with an intense focused laser pulse [9]. They showed that the ponderomotive force limits the effective volume of radiation. Electrons whose initial position is more than one wavelength away from the center of a tightly focused laser can drift out of the laser beam before the peak intensity arrives. As a result, the effective interaction volume can be much smaller than the actual laser focus, limited to a cylinder of radius approximately of $\lambda/10$ [9].

1.3 Experimental History

In 1983, Englert and Rinehart claimed the first experimental observation of nonlinear Thomson scattering [10]. They collided a pulsed neodymium-glass laser with a continuous, low-energy beam of electrons. The laser-beam intensity calculated for that experiment was estimated to be 1.7×10^{14} W/cm^2. They detected second-harmonic photons (532 nm wavelength) using a photo multiplier tube (PMT). Later Iinuma *et al.* expressed skepticism that Englert and Rinehart saw photons arising from actual nonlinear Thomson scattering, given that the laser intensity was far below the relativistic regime.

The first definitive observation of nonlinear Thomson scattering was performed by Chen *et al.* in 1998 [11]. They used a laser system that produced 400-fs duration pulses at an intensity many orders of magnitude higher than that used by Englert and Rinehart. They observed the angular distribution of second and third harmonic photons, which qualitatively matched theoretical predictions of Castillo-Herrera *et al.* [8]. They measured nonlinear Thomson scattering in the equatorial plane surrounding the laser focus and also around a circle shifted to the forward direction from the equator by 39°.

In 2000, Chen *et al.* additionally published experimental observations of phase-matched relativistic harmonic generation. In their experiment, they developed a new theory which describes how phase matching in a plasma can enhance the harmonic radiation [12]. They measured a coherent beam of the third-harmonic from nonlinear Thomson Scattering.

A number of groups have since investigated nonlinear Thomson scattering from energetic electron beams colliding with intense laser pulses, where the scattering is highly directional and extremely blue shifted [13–20]. Surprisingly few measurements of nonlinear Thomson scattering have been made where the lab frame and the electron average rest frame are not dissimilar [10–12, 21, 22].

1.4 Experiments at BYU

We recently preformed experiments at Brigham Young University (BYU) which are similar to those by Chen *et al.* in 1998 [11]. We measured fundamental, 2nd, and 3rd harmonic nonlinear Thomson scattering emitted into the equatorial plane surrounding a tightly focused laser (i.e. in the plane perpendicular to the laser propagation direction). Importantly, we were the first to resolve the scattered light into distinct polarization components. By measuring both polarization components, we were able to definitively demonstrate for the first time the two-dimensional nature of the electron motion, namely, its figure-8 motion. Previous "confirmations" of the figure-8 motion [11, 19] were based on observations that do not distinguish between one-dimensional and two-dimensional motion of the electron [23].

The experimental setup used at BYU is shown in Fig. 1.2. We use an off-axis parabola that focuses 800 nm Ti:sapphire laser pulses to a spot size of $w_0 = 3.2$ μm. The pulses had duration τ = 38 fs and peak intensity 1.5 $\times 10^{18}$ W/cm^2. Alignment of the photon collection system to the tight laser focus is key in our experiment. Inside this tight focus, electrons interact with the high-intensity field where nonlinear Thomson scattering happens. The scattered light from this interaction were imaged onto a 100-micron fiber connected to a photon detector. The measured interaction region in the focus was about 100 microns wide along the path of laser propagation. Alignment is extremely sensitive. Motor actuators are used to aid the alignment in the *x, y* and *z* dimensions with a precision of a few microns.

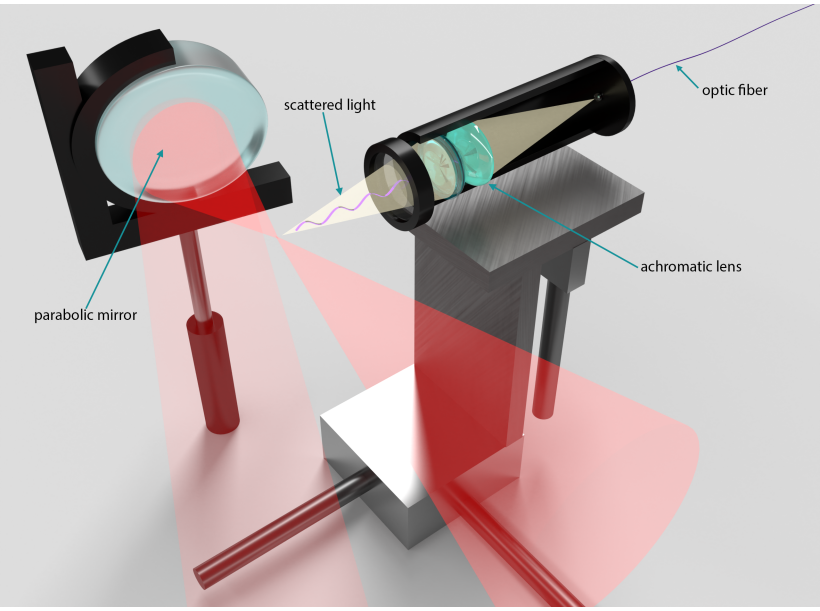

Figure 1.2 Experimental set up to produce and detect nonlinear Thomson scattering. The off-axis parabola (parabolic mirror) focuses the incident laser beam. Scattered photons go through a polarizer, after which an achromatic lens pair focus the signal into an optic fiber.

Electrons for the experiment were donated from low-pressure helium, which becomes ionized by the rising edge of the laser pulse within the interaction region. In order to change the orientation of the linear laser polarization, a half wave plate was rotated in the incident beam prior to the parabolic mirror. This is in principle equivalent to rotating the photon detector around the equatorial plane. Our measurements were restricted to angles around the equatorial plane. Scattered light from the focus passed through a linear polarizer before being collected and focused into a fiber by an achromatic lens pair. The radiation was measured via photon counting. The laser fired at 10 Hz. Fundamental and second harmonic photons were measured using an avalanche photodiode while third harmonic radiation was measured using a photomultiplier tube.

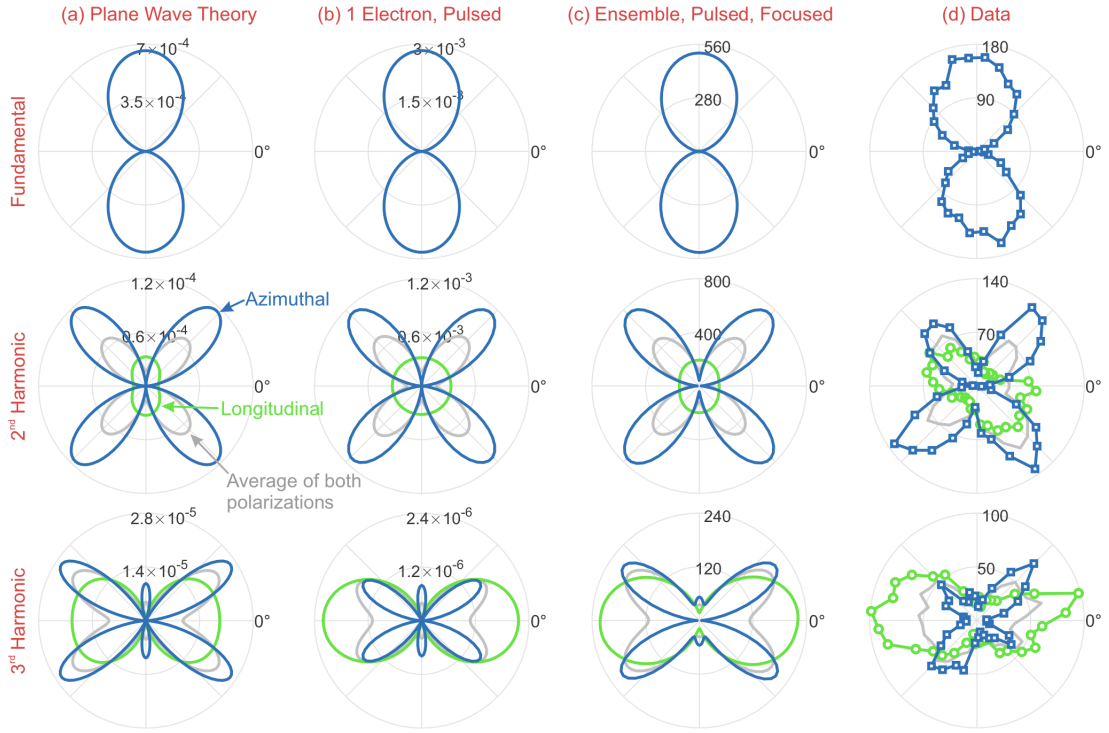

Figure 1.3 Far-field angular emission pattern for first, second and third harmonics, resolved by polarizations along $\hat{\Phi}$ direction (blue) and $\hat{\theta}$ (green). Data is presented as a function of the laser field polarization angle. Column (a) shows the number of photons per steradian emitted during a single laser cycle of a plane wave. Column (b) shows the number of photons per steradian emitted during an entire laser pulse from an electron at the focal center. Column (c) gives the predicted number of photons emitted during 1000 laser shots from an ensemble of randomly distributed electrons, under our experimental conditions. Column (d) shows the number of photons measured in the laboratory. Image taken from Ref. [23]

A comparison of several computational models as well as our experimental results are shown in Fig. 1.3. The radiation patterns for fundamental, second, and third harmonic emitted light are shown for orthogonal polarizations. Calculations for the plane-wave theory in the lectron senter-of-mass frame are shown in column (a). Column (b) shows calculations for a 35-fs plane-wave pulse. Column (c) shows emission computed for an ensemble of randomly distributed electrons in a tightly focused laser pulse, similar to our experimental conditions. Column (c) in Fig. 1.3 may be compared

directly with the measurements in the laboratory shown in column (d). There is reasonably close agreement between our measurements and the prediction of photon counts by our model. Distortion in the measured patterns are shown when compared to our model, which may be an indication of distortions in our focused laser. This could be an interesting line of future inquiry.

1.5 Outline of Thesis Project

My thesis work extends our recent research at BYU in two important ways. 1) We upgraded our Ti:sapphire laser system so that we can achieve up to ten times the intensity in our laser focus. Previously, we had just enough laser energy to reach the onset of nonlinear Thomson scattering, with little margin for error. The increased laser energy makes obtaining the necessary intensity in the focus much less challenging. 2) We rebuilt the detector setup to enable detection of nonlinear Thomson scattering at angles away from the equatorial plane, including angles up to 60° away from the equator. The objective of my thesis project is to present measurements of the emitted radiation in the "Northern" and "Southern" hemispheres of the emission sphere and to compare these with emission at the equator. These measurements of the scattered light are also resolved into orthogonal polarization components.

Chapter two provides a theoretical description of nonlinear Thomson scattering, including how electron trajectories are computed in a tight laser focus. Since electrons are donated by helium during the early part of the laser pulse, a simple ionization model is presented which estimates the intensity at which electrons break free from their atoms before producing Thomson scattering. A description of how to calculate the scattered radiation is also given. The emission from an ensemble of electrons is computed; which are randomly distributed throughout the focus, the scenario in our experiments.

Chapter three describes a recent upgrade to our laser-system and presents the spatial, temporal,

and energy characteristics of our beam. Our rebuilt detection system, with its longitudinal as well as azimuthal adjustment capability, is described as well. As with our previous experiments, photons scattered from the tight laser focus are imaged onto the end of the narrow fiber, which requires care to preserve alignment while the angles are adjusted. A technique for alignment was developed, which is also described in chapter three.

Chapter four presents measurements of second harmonic nonlinear Thomson scattering, obtained for the first time over a large fraction of the emission sphere. We resolve the emission into longitudinal and azimuthal polarization components. The data shows good agreement with the predictions outlined in chapter two.

Chapter 2

Analysis of Nonlinear Thomson Scattering

In order to calculate radiation from free electrons, we must first know how they move in the laser focus. Prerequisite to computing electron trajectories is a detailed understanding of the electromagnetic vector fields throughout the laser focus. A discussion of the laser vector fields, the laser intensity necessary for electrons to break free of their donor atoms, the trajectories of liberated electrons, the radiation that such trajectories produce, and finally the emission from a large ensembles of electrons distributed throughout the focus is reviewed.

2.1 Vector Model of Laser Focus

In 2017, Peatross *et al*. [24] reviewed various vector models of a Gaussian laser beam. They developed a streamlined description of the diffraction integral used for calculating vector fields produced by a uniformly polarized Gaussian beam reflected from an ideal parabolic mirror. They compared various analytical approximate formulas for the vector fields to the results from the diffraction integral. They endorse a model by Erickson and Singh as the best analytical representation of the fields in the focus [24]. This model imitates the beam well in both near and far fields and is numerically quick (convenient) to evaluate when computing trajectories of electrons in a laser focus.

In contrast, resorting to the full diffraction integral for the fields at each point along an electron trajectory would be computationally expensive.

The electric and magnetic fields in the focused Gaussian laser may be adequately represented by

$$\vec{E}(x,y,z,t) = Re\{E_0(\hat{x} + \frac{xy}{2\mathbb{Z}^2}\hat{y} - i\frac{x}{\mathbb{Z}}\hat{z})\psi e^{i(kz-\omega t)}\varepsilon\} \tag{2.1}$$

$$\vec{B}(x,y,z,t) = Re\{\frac{E_0}{c}(\frac{xy}{2\mathbb{Z}^2}\hat{y} + \hat{x} - i\frac{y}{\mathbb{Z}}\hat{z})\psi e^{i(kz-\omega t)}\varepsilon\} \tag{2.2}$$

where $\psi = \frac{z_0}{\mathbb{Z}} e^{-\frac{k\rho^2}{2\mathbb{Z}}}$ is the usual scalar formula for a Gaussian laser beam, which modifies a plane wave traveling in the $\hat{z}$ direction with exponential factor $e^{i(kz-\omega t)}$. The Rayleigh range is given by z_0, and we define $\mathbb{Z} = z_0 + iz$ and $\rho^2 = x^2 + y^2$. The peak electric field at the center of the laser focus is E_0.

We modified the Singh model to account for the turn-on and turn-off of our pulsed laser. The pulse is represented in Eqs. (2.1) and (2.2) by a Gaussian time envelope:

$$\varepsilon = \exp\left\{ -\frac{\left(t - \frac{z+\rho^2/2R}{c}\right)^2}{\tau^2} \right\} \tag{2.3}$$

$R = z + \frac{z_0^2}{z}$ is interpreted as a wave-front radius of curvature, and τ is the pulse duration. The Rayleigh range is connected to the beam radius w_0 through $z_0 = \frac{kw_0^2}{2}$.

2.2 Ionization of Helium

The free electrons in our experiment are supplied by low-density helium in an otherwise evacuated laser focus. The helium is ionized during the rising edge of the laser pulse. Radiation from bound electrons or from the ionization process contribute negligibly to the overall measured scattered-light signal. The photon energy for our 800 nm laser is 1.55 eV, far less than the work function Φ of helium. In a multi-photon process, electrons can be pulled from the atom (or ion) if the electric field

of the laser exceeds the Coulomb binding force. We estimate below the laser intensity necessary to ionize helium.

A bound electron is under the influence of electric fields from both the atom and the laser. Under a "single-active-electron" assumption, an electron feels a hydrogen-like potential as it moves away from the nucleus and any other bound electrons, which we assume remain close to the nucleus while the one electron escapes. The combined potential of the atom and the laser field that the active electron experiences (along the x dimension) is

$$V(x,t) = -\frac{Ze^2}{4\pi\varepsilon_0|x|} - e\,E_0\,x\cos(\omega_L\,t), \tag{2.4}$$

where Z is the charge state of the ion left behind.

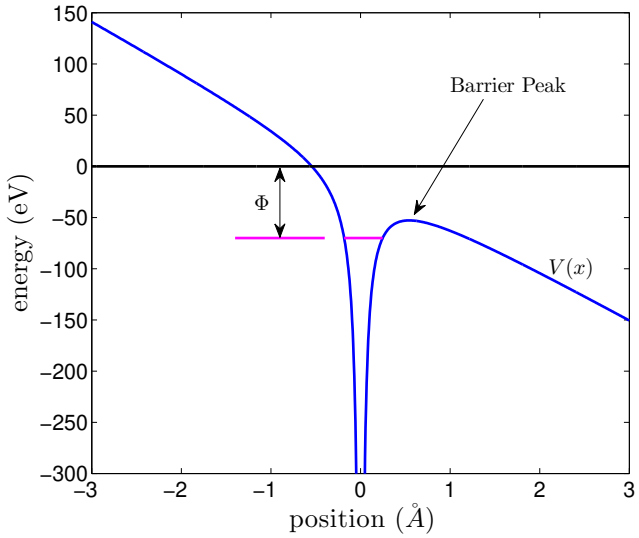

Figure 2.1 Potential energy of a combined Coulombic and laser fields, according for Eq. (2.4) at a moment when $\cos(\omega_L\,t) = 1$.

An estimate of the laser field necessary for ionization is found by calculating the field strength necessary to suppress the barrier until its peak lowers to the binding energy for the electron (i.e., the work function Φ). The maximum suppression occurs when $\cos(\omega_L\,t) = \pm 1$. Setting the derivative

of Eq. (2.4) to zero (with $\cos(\omega_L t) = 1$), we find the location of the peak to be

$$x_{peak} = \sqrt{\frac{Ze}{4\pi\varepsilon_0 E_0}} \tag{2.5}$$

Substitution of x_{peak} into Eq. (2.4) (with $\cos(\omega_L t) = 1$) yields the height of the suppressed potential barrier:

$$V(x_{peak}) = -\frac{Ze^2}{4\pi\varepsilon_0\sqrt{\frac{Ze}{4\pi\varepsilon_0 E_0}}} - eE_0\sqrt{\frac{Ze}{4\pi\varepsilon_0 E_0}} = -\sqrt{\frac{Ze^3E_0}{\pi\varepsilon_0}} \tag{2.6}$$

Thus, the field necessary for over-the-barrier ionization can be computed by setting the peak of the potential barrier to the ionization potential for the electron as follows:

$$\Phi = \sqrt{\frac{Ze^3E_0}{\pi\varepsilon_0}} \quad \Rightarrow \quad E_0 = \frac{\pi\varepsilon_0}{Ze^3}\Phi^2 \tag{2.7}$$

The laser intensity needed to ionize the atom in a linearly polarized field can be computed as

$$I = \frac{1}{2}\varepsilon_0 c E_0^2 = \frac{\pi^2 c\varepsilon_0^3\Phi^4}{2e^6Z^2} \tag{2.8}$$

The accuracy of Eq. (2.8) is remarkably good and predicts the ionization intensity for essentially any atom or ion [25] . In our experiments, the noble gas used in the interaction chamber is helium. The ionization potentials for helium on states $Z = 1$ and $Z = 2$ are 24 eV and 54 eV, respectively. This gives ionization intensities of 1.3×10^{15} W/cm^2 and 8.7×10^{15} W/cm^2, respectively. We assume that the electrons remain attached to helium until the intensity of the laser pulse reaches these values, whereupon the electrons are deemed free to move in the laser field. This provides an initial condition for electron trajectories. As mentioned, this is very early during the laser pulse, given that the peak intensity reaches above 10^{18} W/cm^2.

2.3 Calculations of Electron Trajectories

To calculate an electron trajectory, we insert the electric and magnetic fields of Eqs. (2.1) into the Lorentz force law Eq. (1.1). We then numerically solve the differential equation, subject to the

initial condition dictated by the intensity at which helium releases its electrons. Once free, we assume that the electron no longer interacts with its parent ion. We assume that prior to ionization, the electron emits a negligible amount of radiation. Fig. 2.2 shows the trajectory for an electron initially at the center of a tight pulsed laser focus, linearly polarized in the x direction. The electron experiences a force in the $\hat{x}$ and $\hat{z}$ where the electrons drifts in $\hat{z}$ and oscillates on the $\hat{x}$ direction.

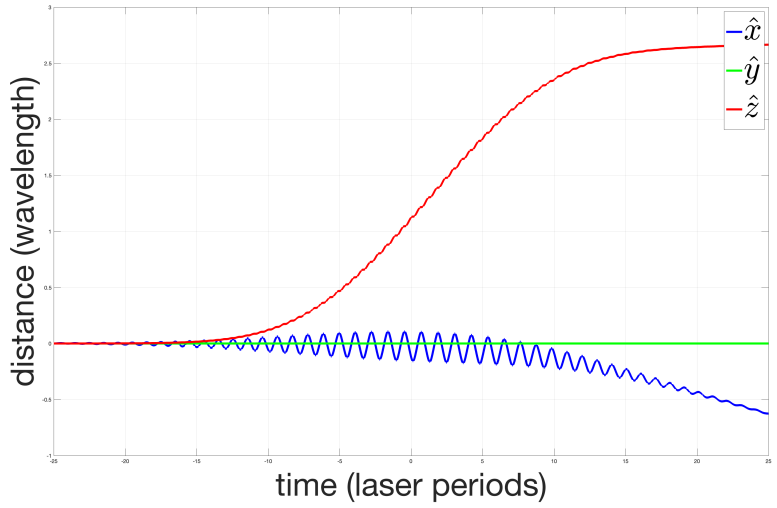

Figure 2.2 Trajectory of an electron centered in the tight focus, each line in the plot represent the electron trajectory in $\hat{x}$, $\hat{y}$, and $\hat{z}$ direction. Simulated by a laser pulse with 2.1×10^{18} W/cm^2 with a pulse duration of 35 fs. For a centered electron, it experiences a force in the $\hat{x}$ and $\hat{z}$ directions where the electron drifts in the $\hat{z}$ direction and it oscillates in the $\hat{x}$ direction

The initial position of the electron within the focus highly influences its trajectory. Fig. 2.3 shows the trajectories of electrons with positions distributed throughout a tight focus. Electrons are seen being pushed out of the focus in many directions as they are also propelled forward in the laser field. Electrons initially positioned close to the axis of the laser focus remain longer in the focus, but they are eventually pushed outward as they simultaneously drift in the $\hat{z}$ direction.

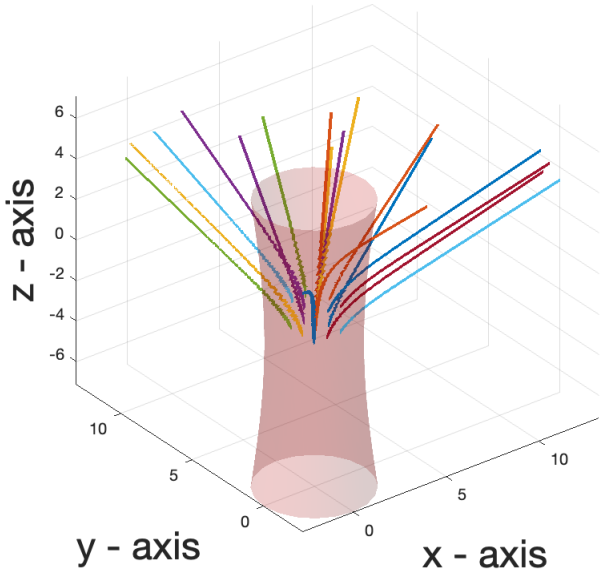

Figure 2.3 Trajectories of an electron positioned at different position along a tight-focus. All distances are in units of wavelength. Peak intensity of 2.1×10^{18} W/cm^2 and pulse duration of 35 fs. Variations in the electron position highly affects the electron trajectory due to the Lorentz force law.

2.4 Calculated Radiation from Individual Electron Trajectories

Suppose that an electron trajectory in a focused laser is described by $\vec{r}\,(t) = x(t)\,\hat{x} + y(t)\,\hat{y} + z(t)\,\hat{z}$, which evolves in time. We might set the origin at the center of the laser focus. The trajectory will have associated velocity $\vec{u}\,(t) = \frac{d\,\vec{r}\,(t)}{dt}$ and acceleration $\vec{a}\,(t) = \frac{d\,\vec{u}\,(t)}{dt}$.

Next, suppose that a detector is located *far* from the focus at position $\vec{r_d} = x_d\hat{x} + y_d\hat{y} + z_d\hat{z}$. The electron will radiate an electromagnetic field. In the *far field*, at detector position $r_d \gg r$, the scattered fields may be expressed as

$$\vec{E_s}(\vec{r_d}, t_d) = \frac{q\,k}{4\,\pi\,\varepsilon_0\,r_d}\,\frac{1}{(1 - \hat{r}_d \cdot \vec{u}/c)^3}\,\hat{r}_d \times ((\hat{r}_d - \vec{u}/c) \times \vec{a}) \tag{2.9}$$

$$\vec{B_s}(\vec{r_d}, t_d) = \hat{r}_d \times \frac{\vec{E_s}(\vec{r_d}, t_d)}{c} \tag{2.10}$$

where the electron position $\vec{r}\,(t)$, velocity $\vec{u}\,(t)$, and acceleration $\vec{a}\,(t)$ are all evaluated at time t. On the other hand, the fields arrive to the detector at a later time $t_d \cong t$, defined by

$$t_d \cong t + \frac{r_d}{c} - \hat{r}_d \cdot \frac{\vec{r}}{c} \tag{2.11}$$

Poynting vector of the scattered radiation is

$$\vec{S}\,(\hat{r_d}, t_d) = \vec{E_s}(\vec{r_d}, t_d) \times \frac{\vec{B_s}(\vec{r_d}, t_d)}{\mu_0} \tag{2.12}$$

From Eq. (2.9), we know that $\hat{r}_d$ and $\vec{E_s}$ are perpendicular. Therefore, the cross product reduces to

$$\vec{S}\,(\hat{r_d}, t_d) = \hat{r}_d\;\varepsilon_0\;cE_s^2(\vec{r_d}, t_d) \tag{2.13}$$

where the energy is directed toward the detector along $\hat{r_d}$.

If we place a linear polarizer in front of the detector, we may resolve the scattered light field into orthogonal polarization components, aligned along, say, either the azimuthal or longitudinal direction in spherical coordinates:

$$\begin{aligned}\hat{\theta} &= \cos\theta\ \cos\phi\ \hat{x} + \cos\theta\ \sin\phi\ \hat{y} + \sin\theta\ \hat{z} \\ \hat{\phi} &= -\sin\phi\ \hat{x} + \cos\phi\ \hat{y}\end{aligned} \tag{2.14}$$

The Poynting flux that transmits through a polarizer aligned along either direction is

$$\begin{aligned}S_\theta &= \varepsilon_0\, c \left(\vec{E}_s \cdot \hat{\theta}\right)^2 \\ S_\phi &= \varepsilon_0\, c \left(\vec{E}_s \cdot \hat{\phi}\right)^2\end{aligned} \tag{2.15}$$

where the total Poynting flux (in the absence of a polarizer) is $S = S_\theta + S_\phi$.

Since the magnitude of the Poynting vector has units of power per area, integration in time yields energy per area delivered to a detector, from the entire pulsed interaction. The energy fluence for each polarization is

$$\begin{aligned}\mathscr{E}_\theta &= \varepsilon_0\, c \int_{-\infty}^{\infty} dt_d\ S_\theta(\hat{r_d}, t_d) = \varepsilon_0\, c \int_{-\infty}^{\infty} d\omega\ S_\theta(\hat{r_d}, \omega) \\ \mathscr{E}_\phi &= \varepsilon_0\, c \int_{-\infty}^{\infty} dt_d\ S_\phi(\hat{r_d}, t_d) = \varepsilon_0\, c \int_{-\infty}^{\infty} d\omega\ S_\phi(\hat{r_d}, \omega)\end{aligned} \tag{2.16}$$

The latter expression is equivalent to the first according to Parseval's theorem, where $S(\hat{r_d}, \omega)$ is computed from the Fourier transform of the scattered field:

$$\vec{E_s}(\vec{r_d}, \omega) = \frac{1}{\sqrt{2\pi}} \int_{-\infty}^{\infty} \vec{E_s}(\vec{r_d}, t_d) e^{i\omega t_d} dt_d \tag{2.17}$$

The motion of the electrons in the laser focus is quasi periodic, so the radiation tends to produce a series of harmonics of the driving field. To see the individual harmonics distinctly, one can apply a spectral window to $\vec{E_s}(\vec{r_d}, \omega)$, setting it to zero outside of a given range of frequencies. Experimentally, this amounts to placing a bandpass filter in front of the detector. For example, to observe the second harmonic, when electrons are stimulated by an 800-nm laser pulse, we place a bandpass filter in front of the detector that transmits wavelengths in the vicinity of 400 nm while blocking other wavelengths.

Because electrons experience an average forward z-drift during the laser pulse, the radiation undergoes red shifting, when viewed from the side of the focus. For example, in our experiments, we observe the second harmonic at 450 nm with a bandwidth of 25 nm.

Fig. 2.4 shows the 1st, 2nd, and 3rd harmonic scattered radiation from an electron initially positioned at the center of a tight focus. The figure represents the far-field intensity over the emission sphere. The radiation is computed for each polarization component, aligned azimuthally and longitudinally, with bandpass filters appropiate for the fundamental, 2nd, and 3rd harmonics. Previously, our group has measured harmonics emitted along the equator of the emission sphere. For my thesis project, I measure for the first time nonlinear Thomson scattering over a wide range of angles on the emission sphere, in both the 'Northern' and 'Southern' hemisphere.

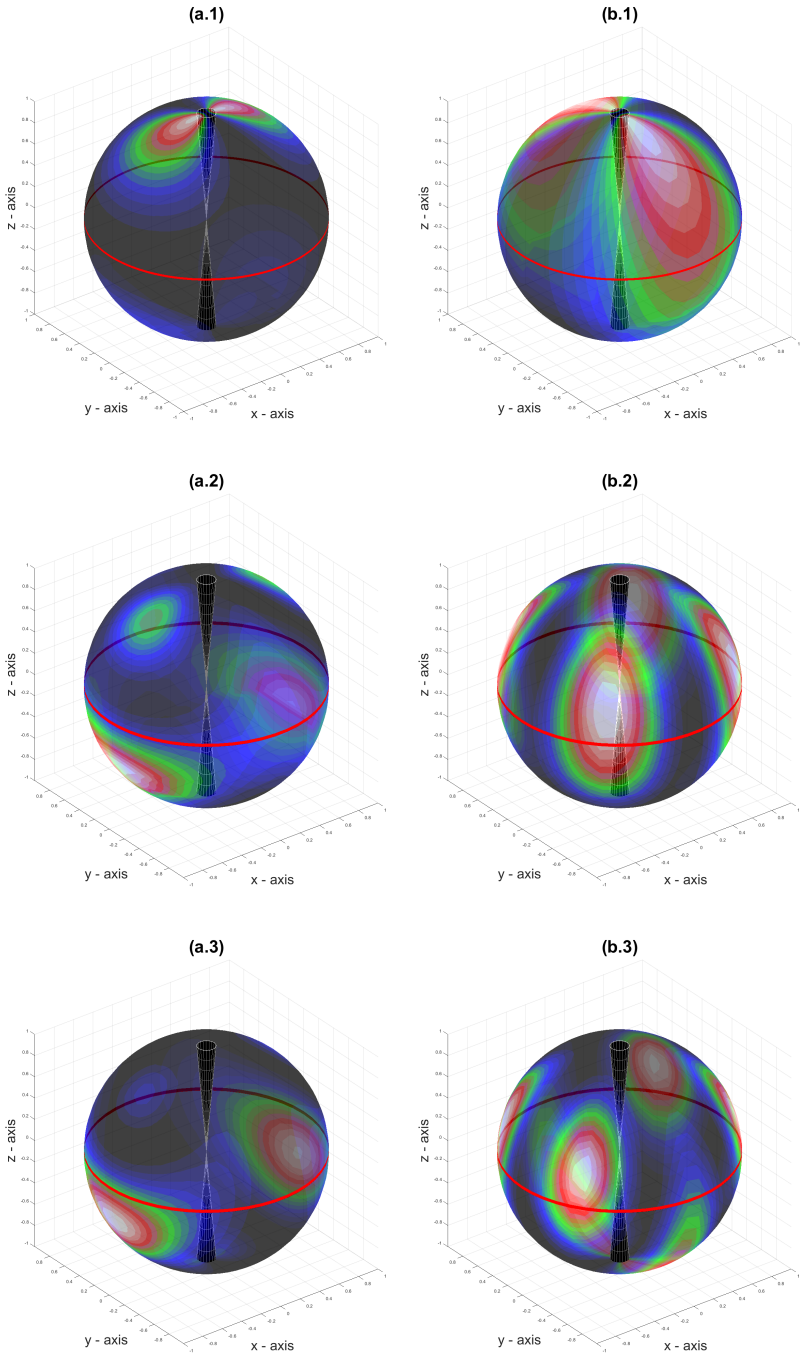

Figure 2.4 Far-field nonlinear Thomson scattering for electrons simulated by a laser pulse with 2.1×10^{18} W/cm^2. Black cones represent the focused laser traveling in the z direction. Radiation pattern is computed and for both polarizations ($\hat{\Phi}$ and $\hat{\Theta}$ directions) of fundamental, second harmonic, and third harmonic. Scattered light is shown in all directions in colored scale from white (hotter) to blue (no radiation). Red line represents the equator of the emission sphere.

2.5 Emission from Electron Ensembles

As was explained in Sect. 2.3, electron trajectories in the laser focus are very sensitive to their initial positions. Electrons typically are propelled out the side of the focus during the course of the laser pulse, which can severely distort the radiation that they scatter. In our experiments, thousands of electrons are randomly distributed throughout the focus, each with a tiny probability of emitting a photon. The electrons are diffuse enough that we may ignore particle-particle interactions. Their random distribution of locations means that the emitted radiation is incoherent. Thus, we may sum the intensity emission patterns produced from many randomly positioned individual electrons to predict the behavior of the large ensembles of electrons in the focus, averaged over many laser shots.

Figure 2.5 shows the emission pattern from 1000 electrons randomly distributed throughout a laser focus. We sum intensities emitted by the individual electrons. Interestingly, while the emission from individual electrons can be strongly distorted, depending on the character of its unique trajectory, the emission from a large ensemble of electrons resembles the emission from a single electron in a plane-wave pulse.

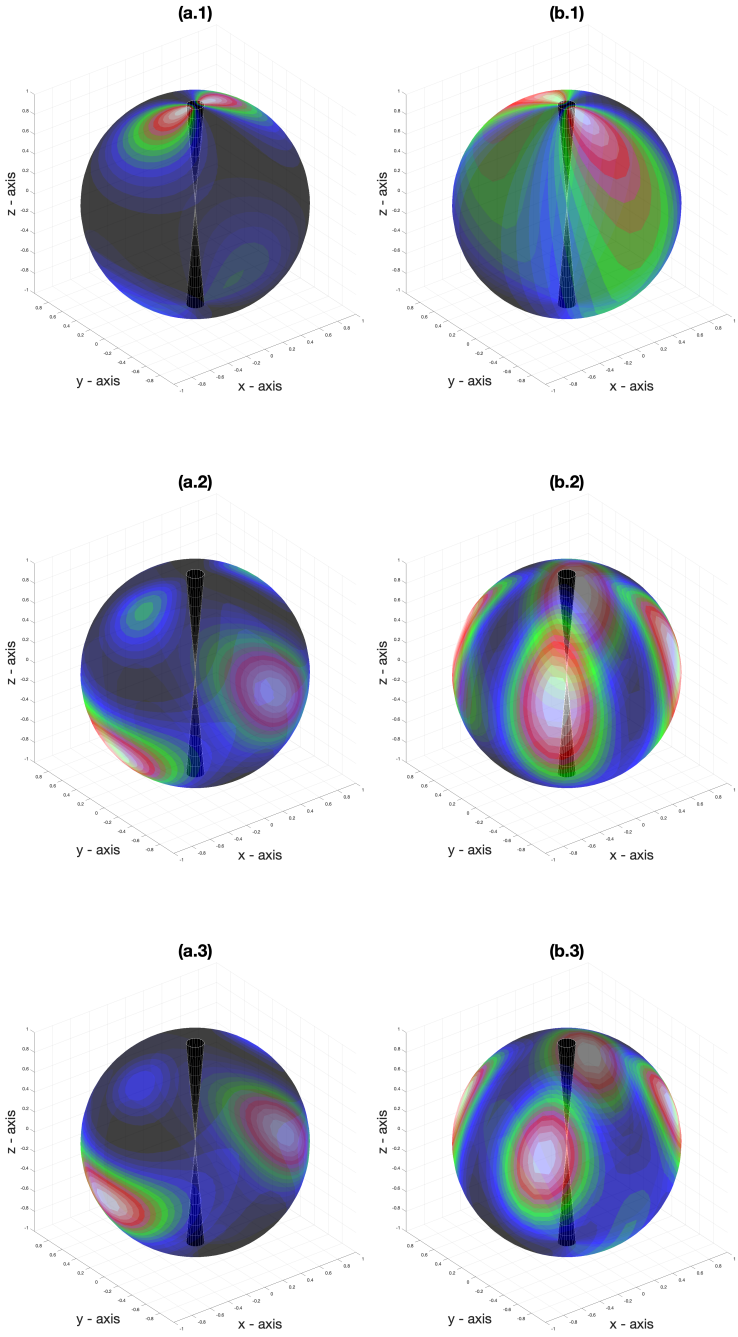

Figure 2.5 Far-field nonlinear Thomson scattering for an ensemble of electrons simulated by a laser pulse with 2.1×10^{18} W/cm^2. Ensemble of electrons is composed of 1000 randomly distributed electrons along the tight focus. Radiation is average from each individual electron is sum and averaged. Laser is traveling in the z direction. Radiation pattern is computed and for both polarizations ($\hat{\Phi}$ (a) and $\hat{\Theta}$ (b) directions) of fundamental (1), second harmonic (2), and third harmonic (3). The average radiation from an ensemble of electrons resembles the radiation of a single electron at the center in a tight-focus.

Chapter 3

Experimental Setup

3.1 Overview of Laser System

For the experiments presented in this thesis, we upgraded our laser system to produce significantly higher pulse energy than available in previous years. We provide here an overview of our Ti:sapphire chirped-pulsed amplification (CPA) laser system. The system consists of several 532 nm pump lasers that provide energy to four Ti:sapphire crystals, which produce and amplify 800 nm laser pulses.

Pulses originate in a Ti:sapphire self-mode-locking oscillator (KM Labs) pumped by a 5 W, 532 nm CW laser (Lighthouse Photonics Sprout). The oscillator produces a pulse train of 15 fs, 800 nm pulses with nanoJoule-level pulse energy. The pulses are temporally stretched to approximately 300 ps. A Pockels cell (PC) then selects a pulse every 0.1 s to be amplified in a chain of three Ti:sapphire amplifiers. Pockels cells isolate the separate amplifier stages and temporally isolate the pulses to be amplified. The Ti:sapphire amplified stages are pumped with two frequency-doubled pulsed Nd:YAG Lasers operating at 10 Hz. The final pulse energy is aboout 300 mJ. After amplification, the pulses are temporally compressed back approximately 35 fs. These pulses are then

sent to an interaction chamber where they are tightly focused into with an off-axis parabola. The resulting free electrons oscillate at relativistic speeds, producing Nonlinear Thomson scattering.

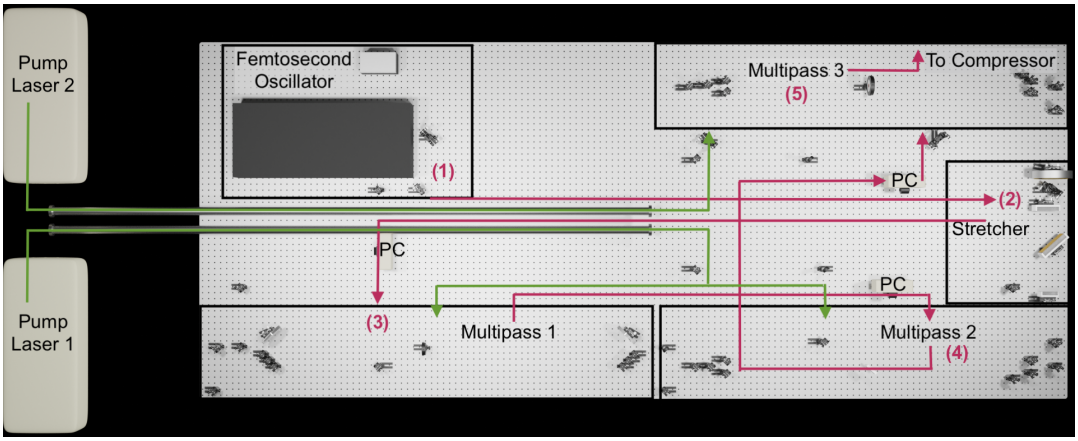

Figure 3.1 Schematic of Ti:sapphire laser system.

.

3.2 Stretcher and Compressor

Before amplification, the pulses that emerge from the oscillator are stretched to approximately 300 ps using a diffraction grating and telescope with focal length $f = 61$ cm. The beam enters the stretcher from an injection mirror. After bouncing from the grating, the beam travels to a concave mirror. It then travels to a flat mirror located at the focus of the concave mirror and returns again to the concave mirror, to form a 1:1 telescope. This telescope introduces an effectively negative distance of $2f$, for an overall (negative) distance of $\ell - 2f$, where ℓ is the distance between the grating and the concave mirror. The beam hits the grating for a second time and then retro-reflects from a flat mirror, which causes the beam to retrace its path with a small vertical misalignment to allow the beam to be picked off instead going back into the oscillator. In the stretcher, the beam spreads out spatially by wavelength, causing a spatial chirp. The spatial chirp is removed when the beam retraces its path, while doubling the induced temporal chirp.

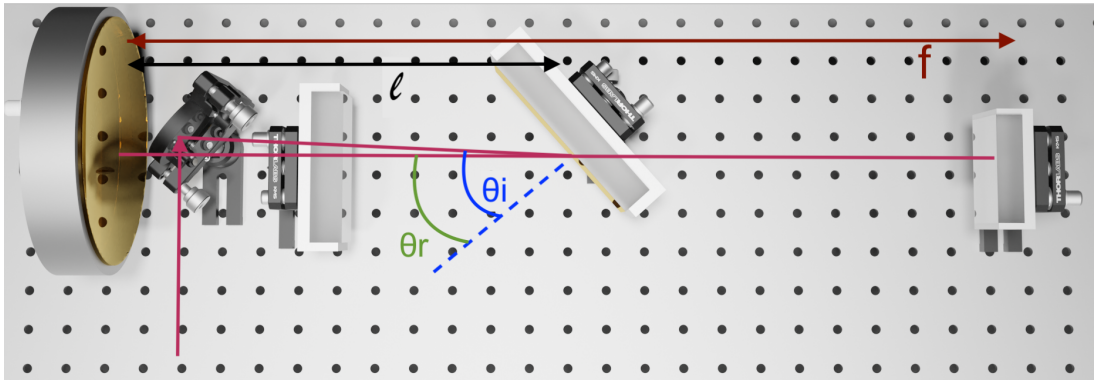

Figure 3.2 Top view of stretcher setup.

The diffraction gratings are gold coated with groove spacing of $d = 1$ mm/1480 and overall width 12.5 cm. Fig. 3.2 depicts the stretcher, which uses a 15 cm-diameter concave parabolic mirror in the telescope. The pulses from the stretcher are reduced in intensity by four orders of magnitude, owing to the increased pulse duration. This significantly reduces the risk of damaging optical components in the amplifiers.

To calculate the duration of the stretched pulse, consider the diffraction angle θ_r as a function of wavelength:

$$\theta_r = \sin^{-1}\left(\frac{\lambda}{d} - \sin\theta_i\right) \tag{3.1}$$

Here, θ_i represents the incident angle of the beam on the gratings. If the input pulse duration is T_{in} (full width at half maximum), the resulting chirped pulse has duration

$$T_{\text{out}} \cong \frac{2\ln 2\ \lambda^2 L}{\pi T_{\text{in}}\ c^2 d^2 \cos^3\theta_r} \tag{3.2}$$

where θ_r is computed for the center wavelength of the pulse (λ = 800 nm). Before upgrading the laser system, our gratings had groove spacing $d = 1$ mm/1200, with incident angle $\theta_i = 31.2°$, and (perpendicular) grating separation $L = 2 \times 30$ cm, where the factor of 2 is to account for the double pass. According to the above approximation, the old stretcher turned a $T_{\text{in}} = 35$ fs into a chirped pulse with duration $T_{\text{out}} = 107$ ps.

Our new gratings have groove spacing d =1 mm/1480, incident angle $\theta_i = 39.4^\circ$, and (perpendicular) grating separation $L = 2 \times 50$ cm. According to the approximation, the new stretcher turns a $T_{\text{in}} = 35$ fs into a chirped pulse duration $T_{\text{out}} = 337$ ps. The new gratings stretch the pulse three times more than the previous gratings, which means three times lower intensity in the amplifiers. This enables us to more easily achieve higher pulse energy while avoiding damage to optical components.

The above estimates of chirped pulse duration are based on a quadratic representation of the chirp introduced by the nonlinear diffraction formula Eq. (3.2). A more accurate calculation of the chirp induced by the old and new grating systems is shown in Fig. 3.3, which is based on the full calculation

$$E(\omega) = \frac{1}{\sqrt{2\pi}} \int_{-\infty}^{\infty} E(t)\, e^{i\omega t} dt \quad \text{and} \quad E_{\text{chirp}}(\omega) = \frac{1}{\sqrt{2\pi}} \int_{-\infty}^{\infty} E(\omega)\, e^{ikL\cos\theta_r} e^{-i\omega t} d\omega \tag{3.3}$$

where $k = 2\pi/\lambda$, $\lambda = 2\pi c/\omega$, and the pulse intensity is proportional to $|E|^2$.

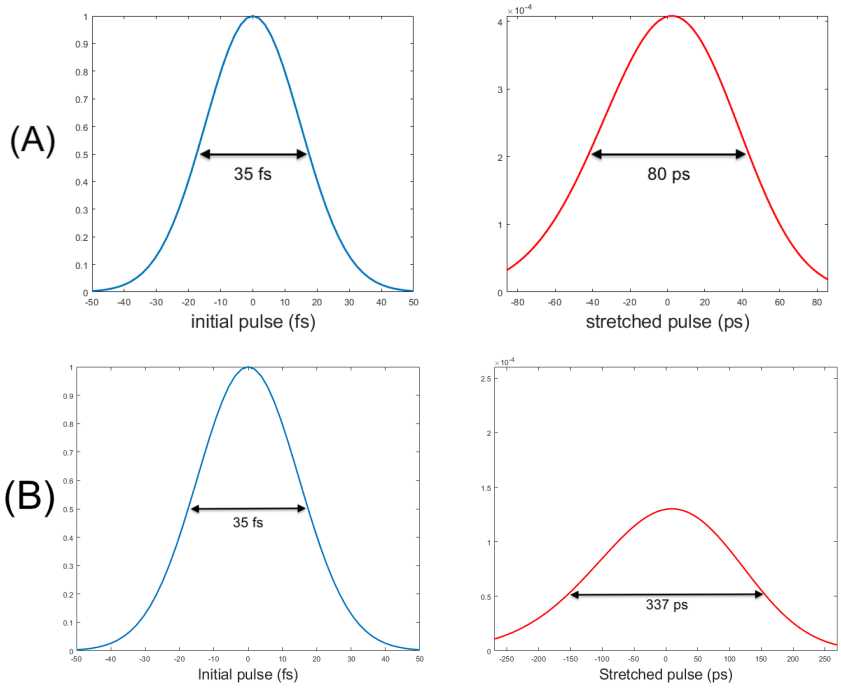

Figure 3.3 The temporal profile of the chirped pulse for the old grating (A) and new grating (B) are shown. An initial 35 fs pulse with a spectral bandwidth of 25 nm is shown. The old grating streched the pulse to 80 ps (A) while the new grating stretched the same pulse to 337 ps (B).

The reason the above calculations were done with 35 fs instead of the 15 fs available from the oscillator is because spectral bandwidth is lost during the amplification process. The final spectrum is only sufficient to make a 35 fs pulse. After amplification, pulses are compressed using a parallel grating pair without a telescope between them (see Fig. 3.4). In this case the separation distance L between them is positive. This undoes the chirp introduced by the negative distance in the stretcher.

The new gratings are about 90% efficient per bounce, whereas the old gratings were only about 75% efficient. After four bounces, this amounts to an extra factor of two in energy available to deliver to the target ($0.9^4 = 66\%$ vs. $0.75^2 = 31\%$).

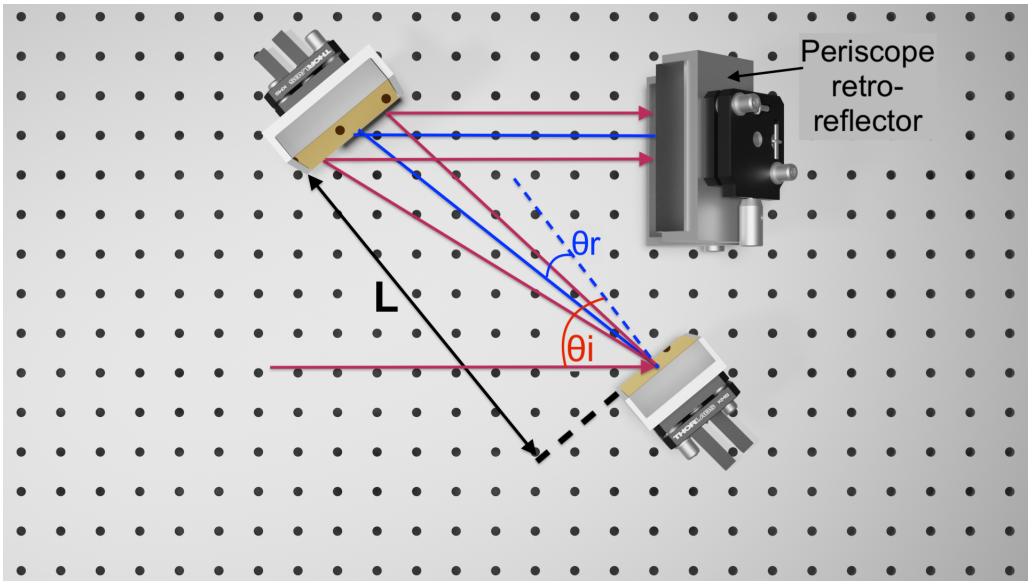

Figure 3.4 Top view of compressor setup.

3.3 Pump Lasers

Three Ti:sapphire amplifier stages are pumped with two frequency-doubled YAG lasers, both producing 532 nm, 10 ns pulses operating at 10 Hz. The first two Ti:sapphire amplifiers are pumped by a Quanta Ray Pro-230, which provides 600 mJ pump pulses. We recently acquired a Quanta Ray Pro-350 laser, which produces 1300 mJ of pump energy, directed into a new 16 mm diameter Ti:sapphire crystal. The pulses from the pump lasers arrive at the amplifying crystals about 20 ns before the 800 nm pulses arrive for amplification. A Stanford Research Systems digital delay generator is used to synchronize the timing.

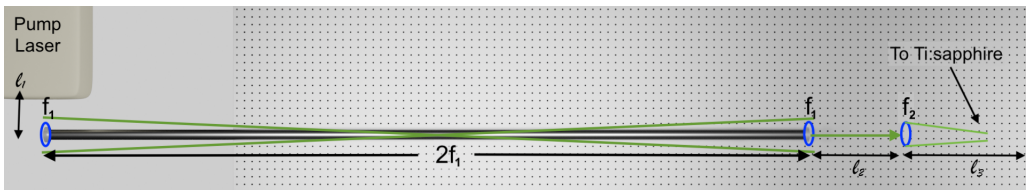

Figure 3.5 Evacuated telescope used for relay imaging of pump lasers.

To achieve the best mode possible in the Ti:sapphire crystals, the pump laser beams are sent through 3 m-long 1:1 telescopes for relay imaging. The telescopes are evacuated to prevent distortion due to ionization of air in the focus that would otherwise occur in the center of each telescope. The telescopes count as negative distances. As the pump beams propagate, they spread and diffract into rings due to the finite aperture of the YAG amplifiers. The best beam mode occurs inside the pump lasers, and the telescopes image this region to the vicinity of the Ti:sapphire crystals for better mode quality.

The pump laser beams are spatially concentrated somewhat onto each Ti:sapphire crystal using long-focal-length lenses that focus the pump light to a point far beyond each crystal. Each crystal is pumped from both sides. The first Ti:sapphire crystal receives approximately 100 mJ on a 1 mm-wide spot. The second Ti:sapphire crystal receives approximately 500 mJ on a 4 mm-wide spot. The third Ti:sapphire crystal receives approximately 1200 mJ on a 9 mm-wide spot.

3.4 Amplifiers

The 800 nm laser pulses go through three Ti:sapphire amplifiers six, three, and three times, respectively, in multi-pass configurations. The multi-pass amplifiers all use flat mirrors at 45-degrees to redirect the beam for each pass. The first amplifier uses large flat mirrors combined with individual small mirrors on each end of the setup. It's Ti:sapphire crystal is pumped the hardest, for a gain per pass of approximately 8, with saturation on the final pass.

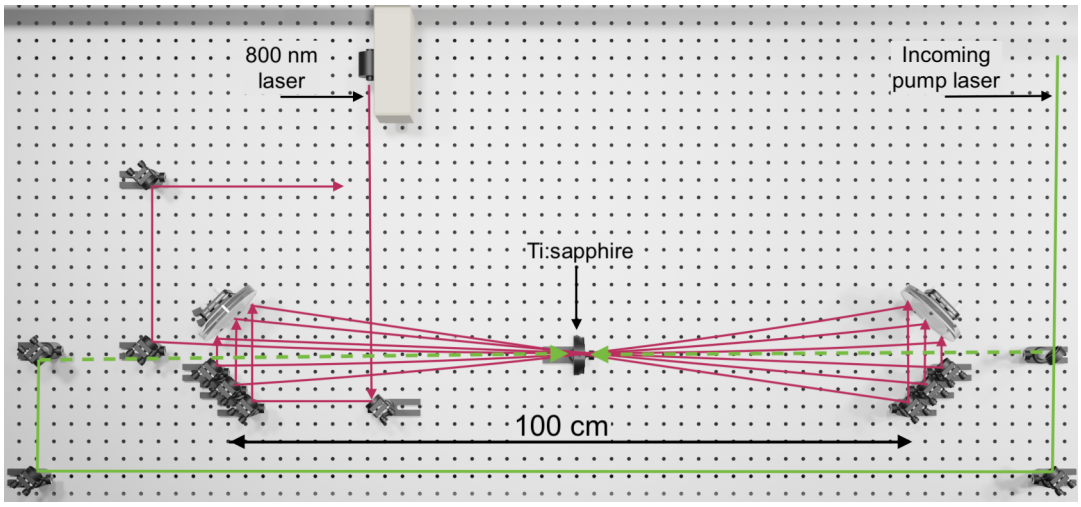

Figure 3.6 Top view of first multi-pass amplifier stage with a total of six passes, achieving 9 mJ output.

Fast-switching Pockels cells and polarizers are used between the first and second amplifiers and between the second and third amplifiers for the sake of temporally cleaning the pulse and isolating the different amplifiers. This prevents reflections from optical components in later amplifiers from sending energy back into the earlier amplifiers where the beams are more concentrated and could damage optical elements.

The second and third amplifiers have similar setups, although we increase the beam diameter from about 4 mm in the second amplifier to about 8 mm in the third amplifier. As seen in Figs. 3.7 and Figs. 3.8, the injected 800 nm beam goes through the Ti:sapphire crystals three times, while being redirected each time by 1"-diameter mirrors at 45 degrees. About 6 mJ makes it through the Pockels cell before the second amplifier. The gain per pass in the second amplifier is approximately 2.5, with saturation on the final pass, reaching about 450 mJ. About 30 mJ makes it through the Pockels cell before the third amplifier. The gain per pass in the third amplifier is also about 2.5, with saturation on the final pass, reaching about 300 mJ.

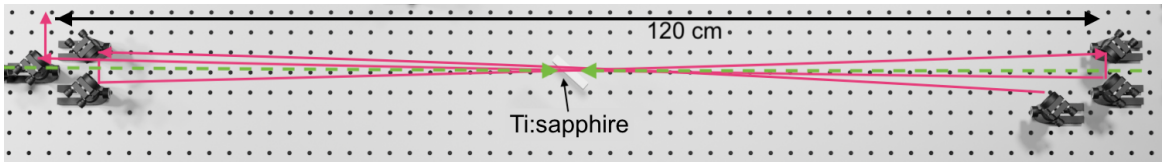

Figure 3.7 Top view of second multi-pass amplifier stage with three passes through a Brewster-cut crystal, achieving 45 mJ output.

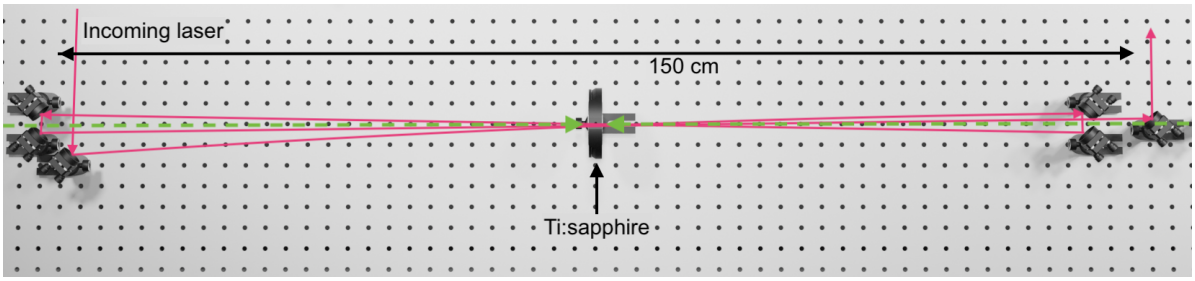

Figure 3.8 Top view of third multi-pass amplifier stage with three passes, achieving 300 mJ output.

A half wave plate and polarizer are used adjust final beam intensity following amplification.

3.5 Laser Beam Spatial Characteristics

As the beam propagates through the series of amplifiers, the spatial quality can degrade. We checked the focusability of the beam after each amplifier stage. To analyze the beam quality, we recorded images of the beam well before and at the focus of a long-focal-length lenses (see Fig. 3.9). The near-field beam profile and the focal length of the lens can be used to predict the ideal focal size, based on diffraction theory. We compare that with the measured focus to determine a percentage for the beam radius over the diffraction limit.

Fig. 3.10 shows vertical and horizontal line outs for each beam seen in Fig. 3.9. Using this data, the predicted beam width was compared to the actual beam width. To calculate the beam width for each picture, the number of pixels was multiplied by the width of each pixel, which is 5.4 μm. The

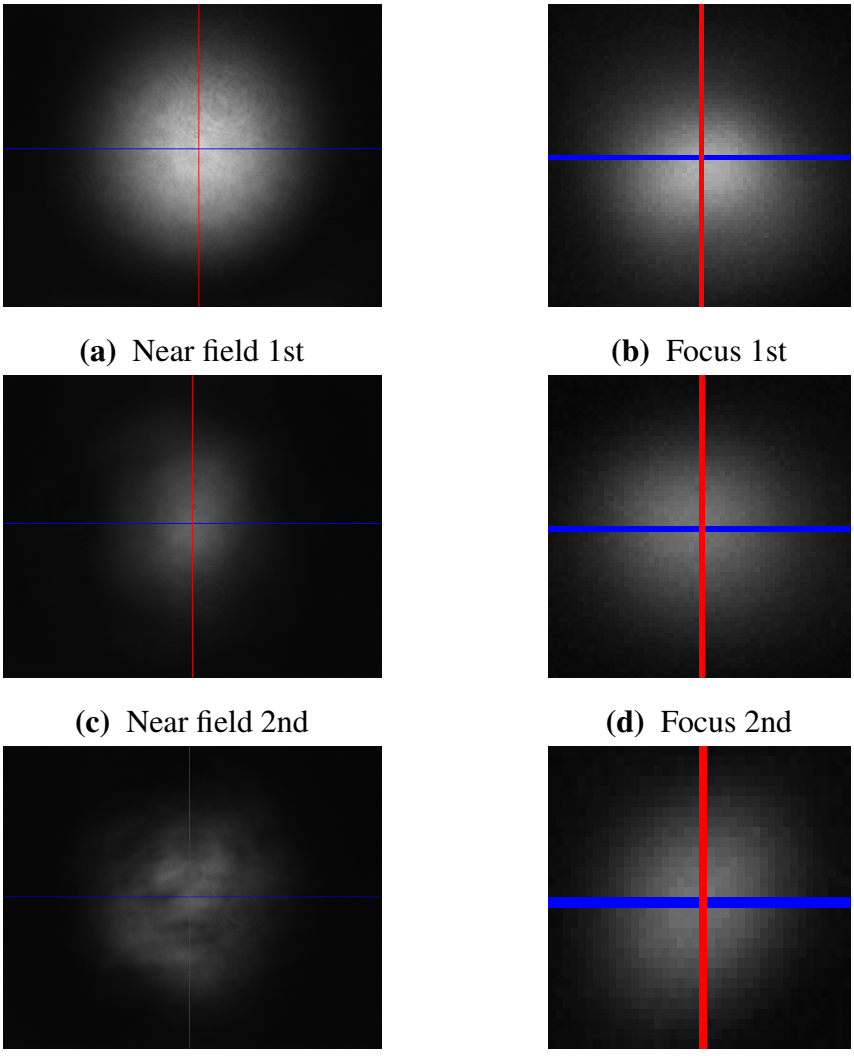

(a) Near field 1st

(b) Focus 1st

(c) Near field 2nd

(d) Focus 2nd

(e) Near field 3rd

(f) Focus 3rd

Figure 3.9 The near field and far field, or focus, images of the beam after each amplifier. The distance between near-field and far-field are 140 cm, 111 cm, and 44cm for the 1st, 2nd, and 3rd amplifier images, respectively.

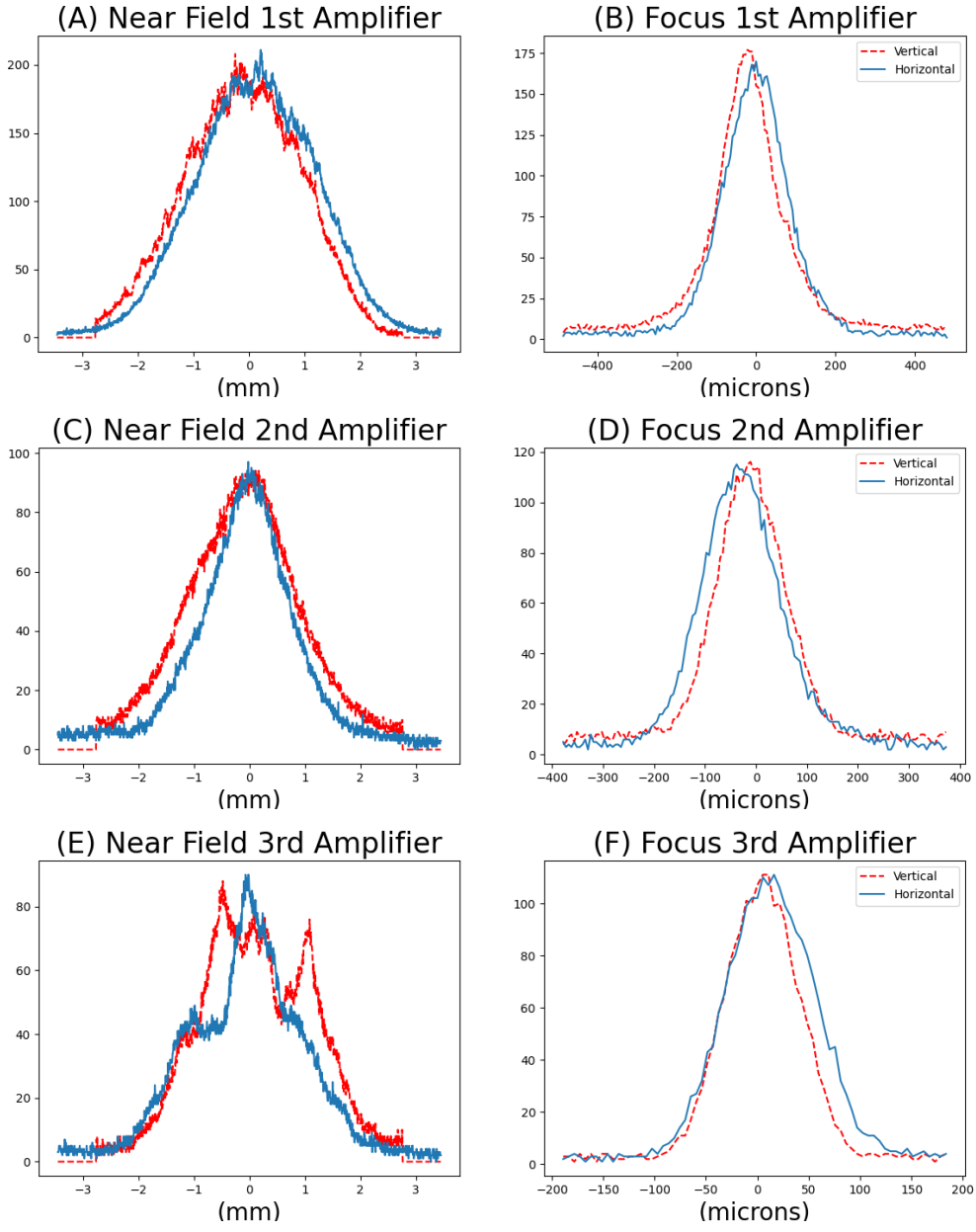

Figure 3.10 Near-field and far-field beam images after each amplifier.

$f\#$ was found in each case by using $f\# = f/D$ with f being the distance of the near-field image in front of the focus, and with D being the diameter of the near-field image.

The predicted diffraction-limited beam waist was calculated using $w_0 = 2\lambda f\#/\pi$ where $\lambda = 0.8\ \mu$m is the wavelength of light. We found that after the 1st and second amplifiers the beam is able to focus to near the diffraction limit. After the third amplifier, however, the beam focuses to 1.3 times the diffraction limit.

3.6 Laser Pulse Spectral and Temporal Characteristics

The spectrum measured before and after the stretcher is shown in Fig. 3.11. When emerging from the oscillator, the pulse contains wavelengths from 740 nm to 860 nm. The stretcher clips some of these wavelengths, so that it range from 760 nm to 850 nm. This is not a concern since the amplifiers narrow the spectrum substantially further.

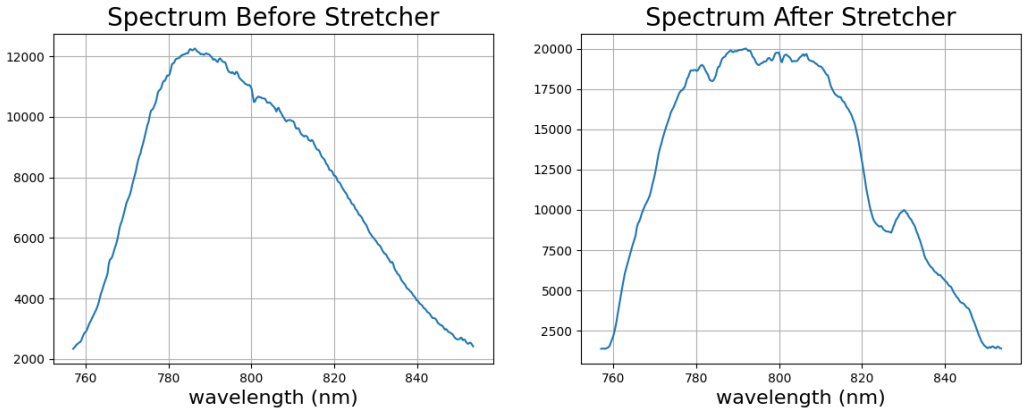

Figure 3.11 The Spectrum of the beam before and after the stretcher.

The spectrum of the pulse changes as it is amplified through the Ti:sapphire crystals. The spectrum measurement after the amplifiers is shown in Fig. 3.12. In a Ti:sapphire CPA system, gain narrowing and redshifting effects can arise as pulses are amplified. Redshifting occurs because the leading edge of the chirped pulse carries the red frequencies, which can receive more gain than the

trailing edge. Saturating the gain too strongly increases the amount of redshifting, which should be avoided [26, 27].

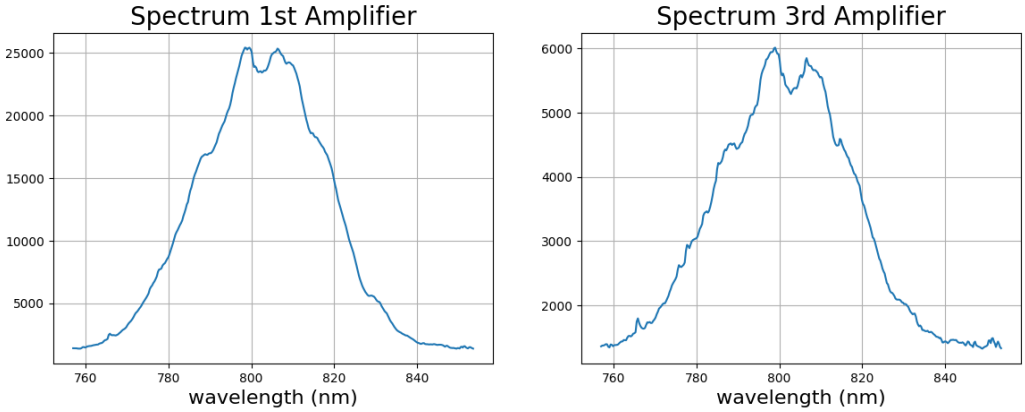

Figure 3.12 The Spectrum of the beam before and after the Amplifiers.

After compression, the pulse duration is measured using auto correlation. The laser beam is split into two identical beams and mixed at a small angle in a KTP crystal. This produces a second-harmonic beam in a nonlinear process [28]. This performs an auto-correlation integral: $sig(\tau) \propto \int_{-\infty}^{\infty} I(t)\, I(t-\tau)\, dt$ where I is the intensity of each identical pulse, t is the time and τ is the delayed time introduced by the crossing angle between the beams and the lateral location in the crystal. The duration of the two identical pulses is mapped into the spatial profile of the harmonic beam. The duration can be calibrated by introducing a known temporal delay into one of the two beams. We measured a pulse duration of our final compressed laser pulse to be about $T_{FWHM} = 35$ fs.

3.7 Peak Laser Intensity

With our laser upgrade, the pre-compressed 800 nm beam has a 5-fold increase in pulse energy. With the improved efficiency of the new diffraction gratings (factor of 2), we have available ten times the energy for experiments. To accommodate the extra energy, the laser beam diameter has

twice the width as it did before. The wider diameter comes a price of worse focusability. Previously, we could focus to about 1.2 times the diffraction limit. After the laser upgrade, we found that we can focus to about 1.5 times the diffraction limit (post compression).

The intensity in the laser focus is given by

$$I = \frac{\mathscr{E}}{T_{FWHM}(\pi w_o^2/2)} \tag{3.4}$$

With $\mathscr{E}$ =200 mJ, T_{FWHM} =35 fs, and $w_o = 4\ \mu$m, we are now able to reach $I = 2\times10^{19}$ W/cm^2. The peak intensity we can achieve is increased between five and ten times. This dramatic improvement enables us to better pursue experiments on nonlinear Thomson scattering. The laser intensity can be varied over a significant range while remaining in the relativistic regime. This allows us to increase the focal-spot size, to increase the pulse duration, or to decrease the pulse energy while remaining in the relativistic regime.

3.8 Photon Collection System

Our previous photon collection lens system utilized 3 translation degrees of freedom. A wire grid polarizer placed in front of the collection lens was used to differentiate azimuthal and longitudinal radiations. The collection lens imaged photons from the interaction region onto the end of a fiber optic. This setup was aligned to the laser focus in the plane perpendicular to it. Our previous experiments on nonlinear Thomson only measured the scattered light along the side of the emission sphere, as indicated by the red lines in Figure. 2.4.

Our previous collection system is depicted in Fig. 1.2, the incoming pulse is focused with an off-axis parabolic mirror. A half-waveplate rotates the laser polarization, effectively allowing rotation of the detector around the equator. In the tight focus, electrons from helium achieve relativistic speeds and radiate different harmonics. Since the electrons have an average forward drift [4], radiation emitted at fundamental frequency is shifted to 900 nm, second harmonic shifted

to 450 nm, and third harmonic shifted to about 300 nm. Bandpass filters restrict the incoming radiation to the harmonic that is being measured. Radiation is registered using either an avalanche photo diode or a photo multiplier tube.

The objective of this thesis is to measure nonlinear Thomson scattering at other angles (*i.e.* away from the equator in the northern and southern hemispheres). In order to achieve arbitrary angles, the collection system was redesigned. Keeping the detector focused on interaction region as it moves to a new angle is a significant challenge. Fig. 3.13 shoes the design of a collection system. The collection lens was mounted over a longitudinal rotational stage, allowing the detector to move away from the equator. While the detector positioning mounts were redesigned, the rest of the collection system remained the same.

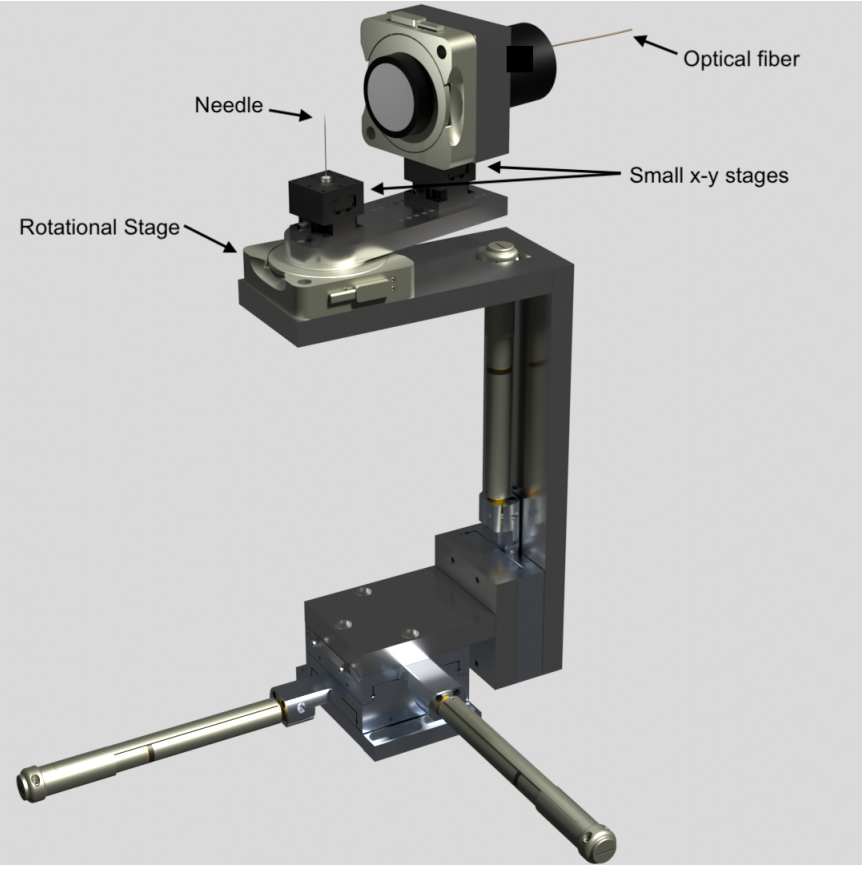

Figure 3.13 Schematic model for new detector setup, which is designed for photon collection at arbitrary angles. The detector must remain aligned to the interaction region as it rotates to different angles.

3.9 In-situ Longitudinal Adjustment of Collection Lens

As the collection lens of our new detector setup moves to new angles, it can easily shift the imaged region away from the interaction region. Although realignment at each new angle is an option, this can be challenging and may lead to errors when attempting to compare relative emission at different angles. Fig. 3.14 provides a visual description of the alignment problem, when the center of the rotation arc does not coincide with the location of the interaction region. It is necessary to center the rotational stage axis directly underneath the interaction region, which has a spatial scale of only 100 micrometers.

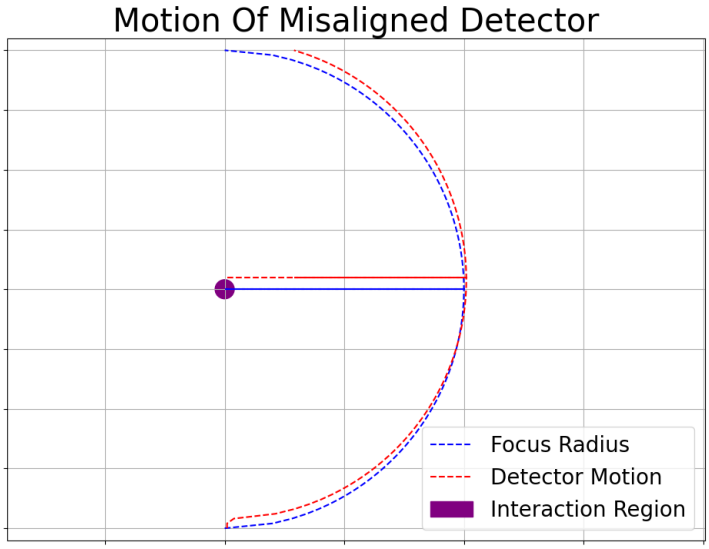

Figure 3.14 Depiction of misalignment of focus to detector motion. The blue dotted line represents the rotational movement needed to stay aligned to the interaction region. The red dotted lines demonstrates what happens with the rotation axis misaligned. Although it is possible to be aligned for some angles, the signal can be lost at other angles.

To center the rotation stage and collection lens system, we minimized misalignment both passively and actively. First, a careful prealignment that was made to the stage. Even with careful prealignment, the system needed slight corrections as data was collected. For this, active alignment

corrections to the focusing system were made during measurements of the radiation.

The approach for passively alignment is depicted in Fig. 3.13. Two small *x-y* stages were added to the setup. The first stage held a temporary needle that was positioned to the rotation axis. A camera observed the needle while the rotation stage moved. The *x-y* stage was incrementally adjusted until the needle did not appear to wobble while the stage rotated. After the needle was aligned to the rotation axis, a second *x-y* stage was used to align the photon collection lens system to the needle. To achieve this, a laser light of 480 nm was sent backwards through the optical fiber. The detector's position was then adjusted so that the focusing laser light struck the needle. Finally the whole setup was moved to the vicinity of the main laser focus using a motorized *x, y, z* translation stages. After proper alignment, the needle was removed.

Active alignment took place when seeking signal from nonlinear Thomson scattering. To do so, the compressed laser was sent to the interaction chamber. Filters where placed in the laser to avoid self-focusing from the nonlinear interaction of air at high intense laser. With air in the chamber, the focused laser produced a spark near the interaction region of the later experiment. The collection lens was aligned to the spark with the motor actuators. The *x, y* and *z* translation stages provided precised alignment of this.

To verify alignment, the fiber optic coming from the collection lens was temporally connected to an spectrometer. We found that a spectral line at 500 nm produced in air was helpful for alignment. Proper alignment was considered to correspond to maximum intensity of the spectral line. Once optimized, the chamber was evacuated and the filters removed from the laser beam to allow it to enter at full power. Helium was introduced into the chamber, typically at about 0.01 torr, and a search for photons from nonlinear Thomson scattering would be made. The position of the *x, y, z* translation stages would adjusted for optimum signal. Then an iterative alignment procedure would be followed, aligning the z translation stage for maximum signal when the detector is at 90 degrees, and the x translation stage for maximum signal when the detector is at 45 degrees. Fortunately, we

found that the vertical stage remained close to optimal when the rotation stage rotated. The detector was rotated and checked for maximum intensity on new angles. Adjustment ranged within a few hundreds of microns.

Chapter 4

Data

4.1 Measurements

Using the apparatus shown in Fig. 3.13 we measured the second harmonic and fundamental with the detector placed at polar angles $\theta = 45^\circ$, $\theta = 60^\circ$, $\theta = 75^\circ$, $\theta = 90^\circ$, $\theta = 105^\circ$, $\theta = 120^\circ$, $\theta = 135^\circ$, and $\theta = 150^\circ$. The laser propagates along direction $\theta = 180^\circ$ and $\theta = 90^\circ$ is emission directly out the side of the focus. At each detector position the laser polarization was rotated using a half wave plate through a full range of azimuthal angles so that we detect signal at azimuthal angles $\phi = 0^\circ$ to $\phi = 360^\circ$ in 10° increments. For these data runs the energy of the high intensity laser was measured to be 150 mJ after the last amplifier, corresponding to about 90 mJ delivered to interaction region in the focus. The laser focus was measured to have a waist of $w_0 = 5$ μm, and the duration of the pulse was measured to be $T_{\mathrm{FWHM}} = 38$ fs. These parameters correspond to peak intensity $I = 5 \times 10^{18}$ W/cm^2. The helium pressure in the focus was set to 2×10^{-2} Torr for second harmonic and 1×10^{-3} Torr for the fundamental.

4.2 Multiphoton Correction

We use an avalanche photodiode for the detector which cannot distinguish the number of photons in a given shot, so we must correct the measured signal for the possibility that some of detection events were actually multiple photon events. The probability of emitting a certain number of photons in a given laser shot is described by the Poisson distribution. This is due to the fact that the photon emission from a given electron in the focus is independently random from emission of a photon from a separate electron and the probability of emitting multiple photons from any single electron is very small.

In a Poisson distribution, the probability of collecting a specific number n photons in a given laser shot is related to the *average* number of photons in a laser shot $\bar{n}$ via

$$P_n = \frac{\bar{n}^n e^{-\bar{n}}}{n!}$$

If losses in the detection system are also independently random (i.e. if the photon from one electron is no more or less likely to be lost before it can be detected than another photon in the same shot), then the Poisson distribution should still properly describe photons arriving at the detector through the lossy channel.

The probability of getting any number of photons (0, 1, 2, etc.) in a laser shot is unity, or in terms of the P_n above:

$$1 = \sum_{n=0}^{\infty} P_n.$$

A perfect photon-number-resolving detector would be able to independently measure each probability P_n by measuring many shots and counting the number of photons in each. However, our photon counters give the same signal (a single "click") when they detect one or more photons. Therefore, the probability that we measure P_m is a sum of the probabilities of getting one or more photons:

$$P_m = \sum_{n=1}^{\infty} P_n.$$

The signal that we want to measure is proportional to $\bar{n}$ rather than P_m. However, $\bar{n}$ can be deduced from our measured probability P_m as follows:

$$P_m = \sum_{n=1}^{\infty} P_n = \sum_{n=0}^{\infty} P_n - P_0 = 1 - P_0$$

Substituting for P_0 from above, we have

$$P_m = 1 - \frac{\bar{n}^0 e^{-\bar{n}}}{0!} = 1 - e^{-\bar{n}}$$

Then, we solve for the average photon rate $\bar{n}$

$$\bar{n} = -\ln(1 - P_m)$$

For our experiment, P_m is given by number of counts that were detected (absent systematic errors). If N is the total number of laser shots and d is the number of shots where one (or more) photons was detected, then the corrected signal S that represents the total number of photons emitted into the detection channel can be approximated as

$$S = \bar{n}N = -N \ln\left(1 - \frac{d}{N}\right) \tag{4.1}$$

We apply this correction to the plotted data below.

4.3 Comparison of predicted data with actual data

Figures 4.1 and 4.2 show our measured data at each of the detector position. Each data is the summation of 600 laser shots and is corrected by Eq. (4.1). For the second harmonic, we used a bandpass filter centered at 450 nm with a 25 nm bandwidth. We estimate that the peak intensity is about 2.1×10^{18} W/cm^2. The emission is measured for both azimuthal $\hat{\phi}$ (blue) and longitudinal $\hat{\theta}$ (red) polarizations.

The collected data shown as data points is compared with a computational model plotted with solid lines. The amplitude of the computational model plotted in the graphs is arbitrary, with the scale chosen so as to overlap the model and the data for comparison of the shapes of the emission patterns rather than comparing the overall amplitude of the measured data to the computational model. The full spatially resolved emission pattern for this computation model is shown in the middle row of Fig 2.5. Each of the data plots represents the emission pattern as one moves around a given "latitude" of the emission "globe".

The first data plot, Fig. 4.1(a), shows measurements taken with the detector placed at polar angle $\theta = 45^\circ$. Recall that $\theta = 90^\circ$ is straight out the side of the focus, so Fig. 4.1(a) shows data for the case when the detector angle is tilted 45° upstream from the side measurements we have typically made in the past. At these upstream detector angles the longitudinal polarized radiation dominates the signal for this wavelength band. As the detector's polar position angle is shifted in the downstream direction in Fig. 4.1(b)-(c) the azimuthal polarization components become dominant and the distinct lobe pattern in the longitudinal emission becomes more rounded. Then in Fig. 4.1(d) we see the emission pattern that we have typically measured in the downstream direction.

In Fig. 4.2 we see plots of the data as the detector's polar angle position is moved in the downstream direction. Notice that the pattern in the longitudinal polarized emission first develops lobes in the emission direction perpendicular to the laser direction (Fig. 4.2(a)) and then develops a second set of lobes along the direction of polarization (Fig. 4.2(b) and Fig. 4.2(c)). The azimuthally

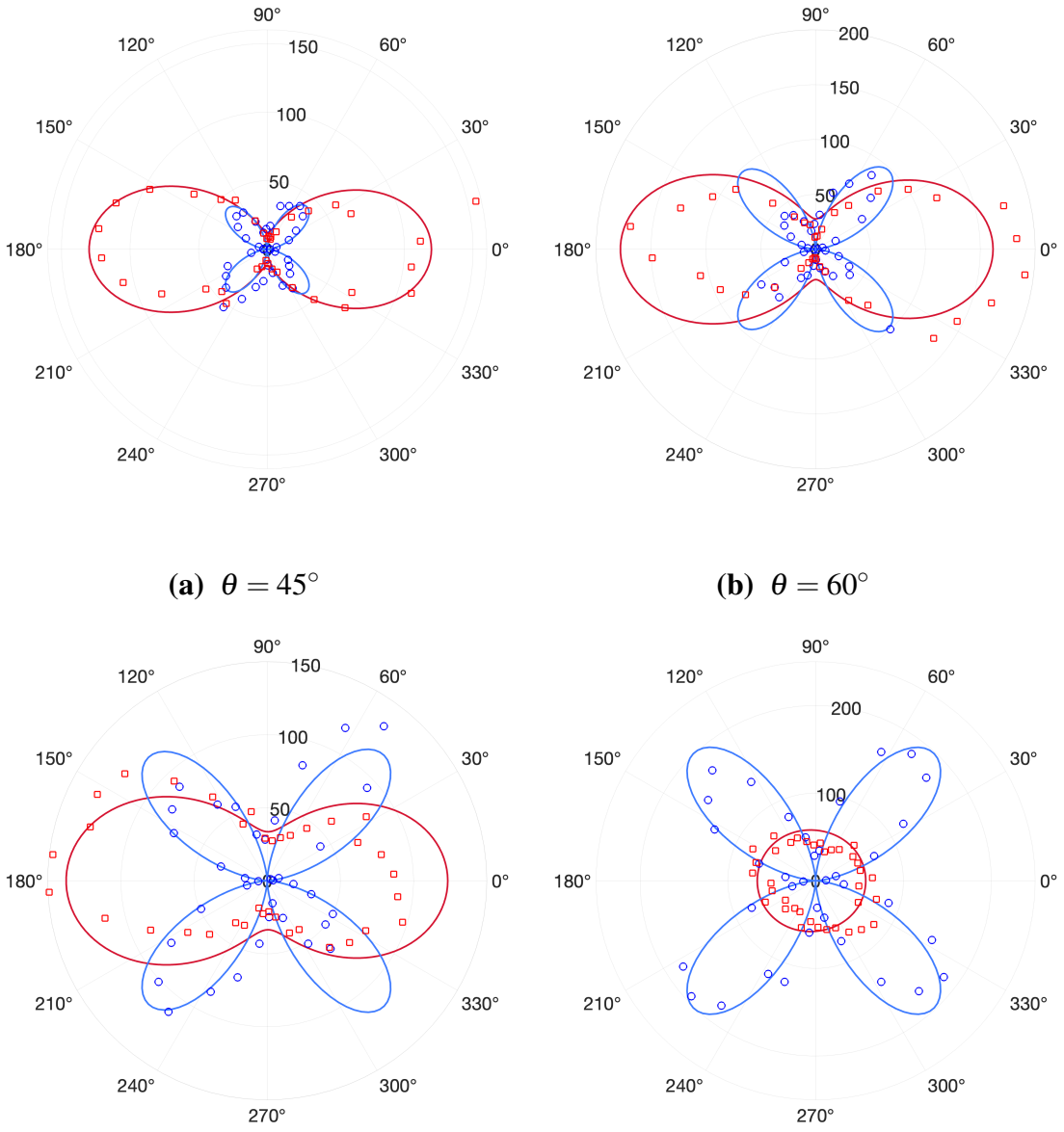

(a) $\theta = 45°$ **(b)** $\theta = 60°$

(c) $\theta = 75°$ **(d)** $\theta = 90°$

Figure 4.1 Comparison of measured second-harmonic photons (points) at $\theta = 45°$ and $\theta = 60°$, $\theta = 75°$ and $\theta = 90°$ to computational model (solid lines).

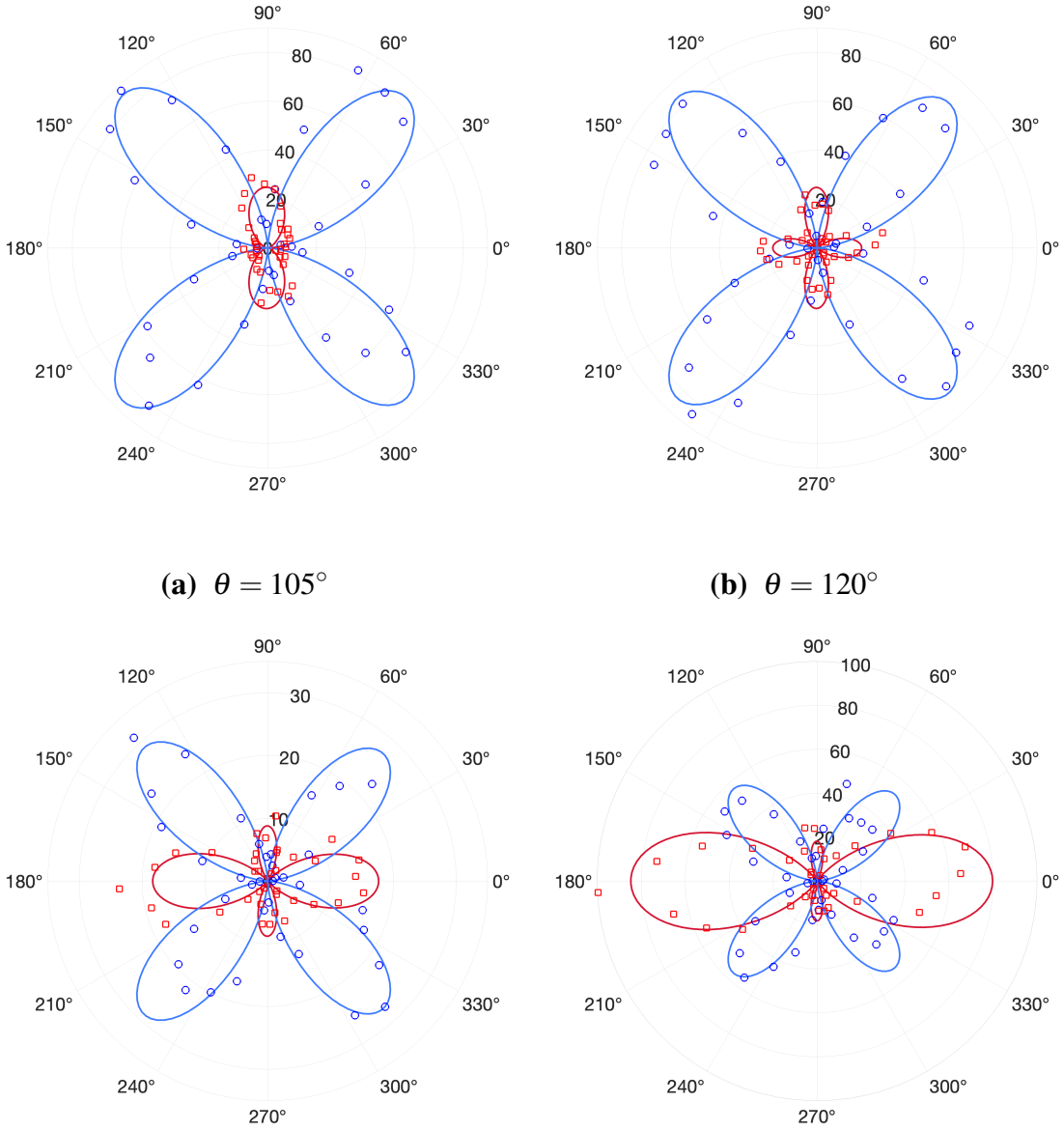

(a) $\theta = 105°$ **(b)** $\theta = 120°$

(c) $\theta = 135°$ **(d)** $\theta = 150°$

Figure 4.2 Comparison of measured second-harmonic photons (points) at $\theta = 105°$ and $\theta = 120°$, $\theta = 135°$ and $\theta = 150°$ to computational model (solid lines).

polarized emission retains its typical clover pattern throughout the change in detection directions from the upstream to the downstream detections angles.

In each of these plots the computational model accurately predicts the shape of the emission and the relative strength of the azimuthal and longitudinal polarization components of the emitted signal. In further study we plan to compare the predicted emission strength with the computational. For the purposes of this thesis, we note that the measured photoemission and the model show good qualitative agreement at each angle. Distortions in the collected data presumably arise imperfections in the laser focus, fluctuations in the laser energy, duration, and focus ability from shot to shot, combined with photon statistics. When the data is compared with the emission sphere seen Fig. 2.4, one can easily see the "continents" in the Northern and Southern hemispheres.

4.4 Conclusions

For the first time, we have measured much of the emission sphere for nonlinear Thomson scattering at the fundamental and second harmonic. In the case of the second harmonic, we see that the "continents" in the Northern and Southern hemisphere are not symmetric. See also Figs. 2.5 and 2.4. This further confirms the figure-8 motion of free electrons as they interact in a high-intensity laser field. Notice that that while executing this motion, electrons traverse the top and bottom of the figure-8 while traveling in one direction while while crossing the middle of the figure-8 while traveling in the opposite direction. In the future, our group plans to also measure the third harmonic over the emission sphere.

The measured radiation patterns that we obtained with our upgraded laser system are relatively symmetrical about the laser axis. This was not the case for previously collected data. See, for example, Fig. 4.1 plot **(c)**, [23], which show deformities in the different "leaves" of the harmonic pattern. The improvement in the symmetry of the new data is likely due improved laser parameters

in the laser focus. We spent much effort to reduce aberrations in the laser beam profile and to align the compression gratings as precisely as possible. The added laser energy may have also played a role. A future line of inquiry might be to study how (intentionally introduced) irregularities in the laser focus might relate to distortions in nonlinear Thomson scattering. This may lead to an improved diagnostic for the performance of focused ultra-high-intensity lasers.

Bibliography

[1] J. Thomson, "Conduction of Electricity," Through Gases, Cambridge (1906).

[2] L. D. Landau, *The classical theory of fields* (Elsevier, 1951), Vol. 2.

[3] Vachaspati, "Harmonics in Scattering of Light by Free Electrons," Physical Review **128,** 664 (1962).

[4] J. H. Eberly and A. Sleeper, "Trajectory and mass shift of a classical electron in a radiation pulse," Physical Review **176,** 1570 (1968).

[5] E. S. Sarachik and G. T. Schappert, "Classical theory of the scattering of intense laser radiation by free electrons," Physical Review D **1,** 2738–2753 (1970).

[6] D. M. Volkov, "Über eine Klasse von Lösungen der Diracschen Gleichung," Zeitschrift für Physik 94 (1935).

[7] E. Esarey, S. K. Ride, and P. Sprangle, "Nonlinear Thomson scattering of intense laser pulses from beams and plasmas," Physical Review E **48,** 3003 (1993).

[8] C. I. Castillo-Herrera and T. W. Johnston, "Incoherent harmonic emission from strong electromagnetic waves in plasmas," IEEE transactions on plasma science **21,** 125–135 (1993).

[9] U. Mohideen, H. Tom, R. R. Freeman, J. Bokor, and P. H. Bucksbaum, "Interaction of free electrons with an intense focused laser pulse in Gaussian and conical axicon geometries," JOSA B **9,** 2190–2195 (1992).

[10] T. Englert and E. Rinehart, "Second-harmonic photons from the interaction of free electrons with intense laser radiation," Physical Review A **28,** 1539 (1983).

[11] S.-y. Chen, A. Maksimchuk, and D. Umstadter, "Experimental observation of relativistic nonlinear Thomson scattering," Nature **396,** 653–655 (1998).

[12] S.-Y. Chen, A. Maksimchuk, E. Esarey, and D. Umstadter, "Observation of phase-matched relativistic harmonic generation," Physical review letters **84,** 5528 (2000).

[13] K. T. Phuoc, A. Rousse, M. Pittman, J.-P. Rousseau, V. Malka, S. Fritzler, D. Umstadter, and D. Hulin, "X-ray radiation from nonlinear Thomson scattering of an intense femtosecond laser on relativistic electrons in a helium plasma," Physical review letters **91,** 195001 (2003).

[14] K. Ta Phuoc, F. Burgy, J.-P. Rousseau, and A. Rousse, "Nonlinear Thomson scattering from relativistic laser plasma interaction," The European Physical Journal D-Atomic, Molecular, Optical and Plasma Physics **33,** 301–306 (2005).

[15] M. Babzien *et al.*, "Observation of the second harmonic in Thomson scattering from relativistic electrons," Physical review letters **96,** 054802 (2006).

[16] T. Kumita *et al.*, "Observation of the nonlinear effect in relativistic Thomson scattering of electron and laser beams," Laser physics **16,** 267–271 (2006).

[17] G. Sarri *et al.*, "Ultrahigh brilliance multi-MeV γ-ray beams from nonlinear relativistic Thomson scattering," Physical review letters **113,** 224801 (2014).

[18] K. Khrennikov, J. Wenz, A. Buck, J. Xu, M. Heigoldt, L. Veisz, and S. Karsch, "Tunable all-optical quasimonochromatic thomson x-ray source in the nonlinear regime," Physical review letters **114,** 195003 (2015).

[19] Y. Sakai *et al.*, "Observation of redshifting and harmonic radiation in inverse Compton scattering," Physical Review Special Topics-Accelerators and Beams **18,** 060702 (2015).

[20] W. Yan *et al.*, "High-order multiphoton Thomson scattering," Nature Photonics **11,** 514–520 (2017).

[21] M. Iinuma *et al.*, "Observation of second harmonics in laser–electron scattering using low energy electron beam," Physics Letters A **346,** 255–260 (2005).

[22] C. He, A. Longman, J. Pérez-Hernández, M. De Marco, C. Salgado, G. Zeraouli, G. Gatti, L. Roso, R. Fedosejevs, and W. Hill, "Towards an in situ, full-power gauge of the focal-volume intensity of petawatt-class lasers," Optics Express **27,** 30020–30030 (2019).

[23] B. Pratt, N. Atkinson, D. Hodge, M. Romero, C. Schulzke, Y. Sun, M. Ware, and J. Peatross, "Experimental confirmation of electron figure-8 motion in a strong laser field," Physical Review A **103,** L031102 (2021).

[24] J. Peatross, M. Berrondo, D. Smith, and M. Ware, "Vector fields in a tight laser focus: comparison of models," Optics express **25,** 13990–14007 (2017).

[25] S. Augst, D. Strickland, D. D. Meyerhofer, S.-L. Chin, and J. H. Eberly, "Tunneling ionization of noble gases in a high-intensity laser field," Physical review letters **63,** 2212 (1989).

[26] H. Hui, J. Zhang, X. Lu, J. Zhang, X. Chen, X. Jiang, B. Zhu, and Z. Lin, "Simulation study of broadband long-pulsed amplification in high-power laser systems," Chinese Optics Letters **14,** 031405 (2016).

[27] F. Wu *et al.*, "Investigations of gain redshift in high peak power Ti: sapphire laser systems," Optics & Laser Technology **103,** 177–181 (2018).

[28] H. Weber, "Generation and measurement of ultrashort light pulses," Journal of Applied Physics **39,** 6041–6044 (1968).